Numerical investigation of bubble dynamics in ageing foams using a phase-field model

Jana Holland-Cunz [b,c,*], Andreas Reiter [a,b], Johannes Hötzer [a,b], Anastasia August [b,c], Michael Selzer [b,c], Britta Nestler [a,b,c]

[a] Institute for Applied Materials MMS, Karlsruhe Institute of Technology (KIT), Straße am Forum 7, Karlsruhe, 76131, Germany
[b] Institute of Digital Materials Science (IDM), Karlsruhe University of Applied Sciences, Moltkestraße 30, Karlsruhe, 76133, Germany
[c] Institute of Nanotechnology (INT), Karlsruhe Institute of Technology (KIT), Hermann-von-Helmholtz-Platz 1, Eggenstein-Leopoldshafen, 76344, Germany

Keywords:
Dry foam
Foam decay
Numerical simulation
Coalescence
Film rupture
Phase-field method

A B S T R A C T

A novel numerical method for simulating liquid foam decay has been developed. This method is based on a phase-field model and captures gas pressure inside the bubbles. It employs an algorithm that includes the spontaneous rupture of foam separating films and coalescence of bubbles. We found that the microstructure evolution in liquid foam in the dry foam limit is predicted. The numerical results demonstrate that the foam ageing dynamics are mapped for the decay process due to successive coalescence events. Moreover, the method is well suited for large-scale microstructure simulations. This allows the investigation of statistical properties of foams, based on the structures' characteristics at the bubble scale. In summary, the method is effective to gain insight into the impact of fundamental factors controlling the evolution and dynamics of decaying liquid foam.

1. Introduction

In many industrial processes and engineering applications, foams are highly valued as a very versatile materials class, as they feature a broad range of properties [1]. These resulting effective properties essentially depend on the microstructure. Therefore, understanding microstructure evolution is key to tailor made materials and components.

Different applications require a different distinct set of effective properties, such as mechanical or thermal characteristics, to achieve the optimum composition. Thus, the configuration of the microstructure determines the specific properties suited for each application. The particularity of the manufacturing process is that the resulting structure and its resulting properties can be precisely tailored based on the microstructure. Targeted production of materials with suitable properties can avoid the uneconomical and wasteful production of materials with unsuitable properties. This correlation is crucial in the manufacturing method of foam templating. In this technical process, liquid foams serve as precursors for creating solid macroporous structures.

Structural features like bubble volume and bubble volume distribution, the degree of order, and bubble connectivity exert large control over most of the resulting properties of the solid foams, e.g. regarding stiffness [2]. Therefore, in order to ensure optimal suitability for specific cases or technical requirements, and to harness effective properties tailored to each application, the templating process provides access through the tuning of these structural characteristics. This tailoring of the liquid precursor structure facilitates access to the resulting properties. The templating route itself is refined by tailoring the structures, and, consequently, the properties. A particular challenge lies in the fact that different parameters affect the effective properties in diverse ways. To unravel this complex structure-properties link, systematic studies on the relationship between structure and property prove invaluable in identifying the optimum structure. As basis to tune the properties in templating and processing routes, it is important to identify the influence of the individual characteristics on the bubble scale.

An enhanced prediction of the morphology improves industrial processes and helps in achieving materials with pre-defined properties [3]. The prediction of morphology requires considering liquid foams to be metastable systems undergoing decay with time. This decay behaviour of liquid foams is complex, due to the interaction of various effects at different length and time scales [4]. Film rupture and bubble coalescence play an important role in the decay process of dry foams, in which the liquid fraction is low. The connection between the stability of individual foam films and the behaviour of a macroscopic 3D foam is still not fully established [5].

Implications for the prediction of foam structures are usually concluded from experimental investigations.

* Corresponding author at: Institute of Nanotechnology (INT), Karlsruhe Institute of Technology (KIT), Hermann-von-Helmholtz-Platz 1, Eggenstein-Leopoldshafen, 76344, Germany.

E-mail address: jana.holland-cunz@kit.edu (J. Holland-Cunz).

Various statistical properties have been investigated in both mono- and polydisperse 2D foams, using different experimental approaches, for example using optical observation. Imaging techniques include, inter alia, fluorescence microscopy [6], imaging via commercial webcam [7] with the aim of recording quantitative evolution. Similarly, Roth et al. [8] report on coarsening dynamics observed via photographs.

Three governing mechanisms can be identified to contribute to foam ageing [9]. First, drainage — under the influence of gravity, second coarsening — gas transfer between bubbles, and third coalescence — rupture of the separating film. Even though these three processes are known to determine the dynamical evolution of foams, a problem remains: Breaking down the contribution of separate, isolated processes to the overall structure formation is difficult. A solution to investigate the individual processes, is to suppress other contributing mechanisms. Different approaches have been proposed. An overview on sophisticated experimental designs is given by Rio et al. [5]. For example, Deminiere et al. [10] study the evolution process dominated by coalescence in a model material (emulsion); Carrier and Colin [11] relate the occurrence of coalescence to the liquid fraction; and Forel et al. [12] track individual coalescence events using a high-resolution camera and conclude on the coalescence probability being proportional to the separating film size. However, there are remaining problems. While drainage and coarsening can be modelled and have been studied to a significant degree, coalescence remains less understood [13]. Foam decay primarily is governed by the characteristics of single films. As a result, the main experimental and theoretical focus has been on investigating the rupture of isolated, single foam films in uncomplicated geometries [14]. Approaches have been pointing towards destruction of single foam films [15], and coalescence with focus on topological rearrangements [16]. Many experiments are conducted with 2D foam structures, as they are easier to handle [8] and 3D experiments are more expensive and complex to capture, often presenting technical challenges.

Probing of isolated ageing processes can be performed utilizing numerical simulations. Achieving accurate representation of the overall topological evolution and scaling behaviour is a crucial aspect in numerical simulations of foam structures [17]. Computational models for evolving foams have been proposed with different points of focus. Kelager et al. proposed their method with the purpose of physically representing 2D foams for computer graphics applications [18]. Other 2D models for the evolution of dry foams, have the aim of a physical representation, and model both coarsening and coalescence. Here, the finite-element based tool Surface Evolver by Brakke [19], proved to be a popular tool for treating complex foam geometries. The model of Chae et al. [17] based on a combination of mass transfer, vertex movement, and edge relaxation also captures surface tension and tracks edges. Kern et al. [20] proposed their viscous froth model, simulating 2D evolution, to describe the dynamics of foam under viscous drag forces on the moving Plateau borders. Recent approaches based on the immersed boundary method are used to investigate 2D statistical behaviour of dry foam [21]. This model captures coarsening in the dry foam limit. Saye's model deals with the different time and length scales of processes with a set of multiscale interlinked algorithms [22], with the result of remarkable representations of foam dynamics. Still, many approaches are associated with the need for complicated mesh generation or interface tracking, and therefore cause high computational effort. Thus, often macroscopic foams are not resolved in the numerical experiments.

In recent years, the phase-field method proved to be a versatile method for simulating the temporal evolution of structures and the course of interfaces, for various application fields in materials science. The method allows for numerical treatment on arbitrary grids due to the approach of diffuse interface modelling, avoiding complicated mesh generation to resolve the foam structure. Complex topologies can be considered using a Cartesian grid, providing large flexibility. In the context of phase-field modelling, a multi-phase-field model to simulate the structure evolution of a dry 2D foam was proposed by Uehara [23]. The model captures both disproportionate gas transfer and coalescence at the same time, but does not take into account gas pressure. The multi-phase-field model for microstructure formation in metallic foams by Vakili et al. [24] facilitates the simulation of foam structure formation with controlled coalescence, for wet foams with high liquid content. Lavoratti et al. [25] present a modified phase-field model and show numerical studies of the dynamics of flowing 2D foam, but do not account for film rupture and coalescence. However, foam representation remains restricted and is not yet fully resolved, such as foams in the dry limit, or statistically and experimentally relevant domain sizes of macroscopic foams. Additionally, the gas pressure inside foams remains to be considered and validated. Thus, the need arises for both a physically realistic computational model and the possibility to simulate macroscopic 2D and 3D foams. Successive coalescence in liquid foams exerts effects on the structure formation, but its impact has not been investigated in detail for foams in the dry foam limit as an isolated decay process independent of the others. To address an improved representation of foam ageing in a numerical model, we aim towards a refined method.

Here, we report the development and validation of a numerical method based on a phase-field model which captures gas pressure inside the bubbles.

A numerical solver based on the PACE3D framework [26], where the presence of a gaseous phase has previously been applied [27], is introduced. Our proposed micro-scale approach employs an algorithm that models the ageing of foams by including the spontaneous rupture of foam separating films and coalescence of bubbles. Notably, we model the occurrence of these events as a purely stochastic process, as proposed in works [12,17]. The approach accounts for gas being treated as a compressible gas, following ideal gas law. A validation of the approach based on simulation results is performed. At its core, the method facilitates a seamless connection between the stability of individual films and the structural formation of the entire foam, allowing for a comprehensive analysis of foam behaviour. Knowledge of the foam behaviour thus contributes to improved control over manufacturing processes. It has been constructed specifically for dry foam, where most of the volume is attributed to its gas phase. By employing the method, we establish the foundation for enhancing foam characteristics, such as the development of foams with predictable morphologies. This provides a pathway towards the production of foam structures with predefined resulting properties. It is a particular advantage of the approach that properties causing inhomogeneities in experimental studies can be excluded explicitly. To guarantee the homogeneity of the foam properties, gravity forces and inter-bubble gas transfer are excluded in the presented method and study. Through numerical validation and exploration of different dry foam structures, we confirm the reliability of the model. To demonstrate its versatility and the ability to effectively map foam decay, the presented method is applied to conduct parameter studies. Different starting morphologies are generated, initial structures include quasi-mono- and poly-disperse configurations with defined degrees of disorder. Using 2D simulations of foam microstructure, we show the applicability of the newly developed algorithm to resolve the temporal evolution.

Foam evolution under various dynamic conditions is investigated in simulation studies, under consideration of the bubble ensemble rearranging. Based on large-scale microstructure simulations, a detailed investigation on bubble statistics is conducted, comprising ensemble values of volumes, gas pressures, bubble shape and connectivity. The results indicate the ability of the method to comprehensively treat coalescence dominated foam decay. The extended model can also be applied to various foam geometries.

2. Modelling ageing foam with the phase-field method

Foam ages under successive coalescence events of bubbles triggered by rupture of the separating film, as well as under the relaxation of the structure into an energetically favourable state. The energy of a foam depends directly on the interfacial area separating bubbles, due to surface tension. From a modelling point of view, the evolution can be regarded as a minimization of the surface energy of the structure.

We propose a basic model to describe foam ageing that takes into account spontaneous film rupture associated with successive coalescence of pairs of gas bubbles. This modelling approach is based on an Allen-Cahn phase-field model formulation [28]. The herein presented formulation includes an energy density contribution, ensuring the assignment of gas pressures to physical phases following the ideal gas law.

2.1. Thermodynamic description

We consider a compressible gas surrounded by an incompressible fluid in a two- or three-dimensional domain $\Omega \subset \mathbb{R}^2$ or $\Omega \subset \mathbb{R}^3$, respectively. The gas is partitioned into cells by foam films, defined by the interface between cells.

The phase-field $\boldsymbol{\phi}(\boldsymbol{x},t) = \left(\phi_1(\boldsymbol{x},t), \phi_2(\boldsymbol{x},t), \dots, \phi_N(\boldsymbol{x},t)\right)$ contains the set of N order parameters ϕ_α, which are continuous components. The indices α, β indicate N different distinct physical phases that are clearly distinguishable. Assuring $\sum_{\alpha=1}^{N} \phi_\alpha = 1$ at each spatial position, the phase-field order parameters can be interpreted as volume fractions of the corresponding physical gaseous and liquid phases. As the order parameters ϕ_α vary continuously between 0 and 1, there is a finite region between the phases, where the interface is diffuse. In this region, phases coexist. Due to the continuous variation of the order parameter, the composition of physical properties changes smoothly, proportional to the composition of the phases. The location of the foam separating film between the phases α and β is defined at the position where $\phi_\alpha = \phi_\beta = 0.5$. As the boundary is implicitly defined and evolves freely, neither interface tracking nor solving of complex boundary conditions is necessary.

For our investigation, the total free energy functional on the domain Ω is taken as

$$\mathcal{F}(\boldsymbol{\phi}, T, \boldsymbol{V}, \boldsymbol{N}) = \int_\Omega \left(\epsilon a(\boldsymbol{\phi}, \nabla\boldsymbol{\phi}) + \frac{1}{\epsilon} w(\boldsymbol{\phi})\right) \mathrm{d}\Omega + \sum_{\alpha=1}^{N} F_\alpha\left(T, V_\alpha(\boldsymbol{\phi}), n_\alpha\right). \quad (1)$$

Here, the positive parameter ϵ is a scaling parameter governing the width of the diffuse interface region, with smaller values of ϵ leading to thinner interfaces. The functional consists of two distinct parts. The first part is composed of the densities of the two interface-controlling terms, $\epsilon a(\boldsymbol{\phi}, \nabla\boldsymbol{\phi})$ and $1/\epsilon\ w(\boldsymbol{\phi})$, which, taken together, represent the surface energy between the different phases. The first quantity relevant to the interfacial energy is the gradient energy density $\epsilon a(\boldsymbol{\phi}, \nabla\boldsymbol{\phi})$, which is formulated as

$$a(\boldsymbol{\phi}, \nabla\boldsymbol{\phi}) = \sum_{\alpha<\beta} \gamma_{\alpha\beta} |q_{\alpha\beta}|^2, \quad (2)$$

where $\gamma_{\alpha\beta}$ is the surface tension between two bubbles, and $q_{\alpha\beta} = \phi_\alpha \nabla\phi_\beta - \phi_\beta \nabla\phi_\alpha$, according to [28]. The second term represents a surface free energy density, which is chosen as a multi-obstacle potential of the form

$$w(\boldsymbol{\phi}) = \begin{cases} \frac{16}{\pi^2} \sum_{\alpha<\beta}^{N} \gamma_{\alpha\beta}\phi_\alpha\phi_\beta + \sum_{\alpha<\beta<\delta}^{N} \gamma_{\alpha\beta\delta}\phi_\alpha\phi_\beta\phi_\delta & \text{if } \phi_{\alpha,\beta} \in [0,1], \\ \infty & \text{else,} \end{cases} \quad (3)$$

and $\gamma_{\alpha\beta\delta}$ is a term introduced to avoid the occurrence of spurious third-phase contributions in two-phase regions.

The second part of the free energy density is obtained from the summation over the integral free energy contributions $F_\alpha\left(T, V_\alpha(\boldsymbol{\phi}), n_\alpha\right)$ for each phase, and accounts for the remaining energetic contributions – i.e. without the surface energy – of the gas within each bubble. Besides the temperature T and the amount of substance n_α as fixed parameters, this bulk energy density contribution indirectly depends on the phase-field $\boldsymbol{\phi}$ through the definition of the volume V_α corresponding to each phase.

In its simplest form, this volume can be defined as

$$V_\alpha(\boldsymbol{\phi}) := \int_\Omega \phi_\alpha(\mathbf{x})\, \mathrm{d}\Omega. \quad (4)$$

More generally, using weighting functions $h_\alpha(\boldsymbol{\phi})$ such as $h_\alpha(\boldsymbol{\phi}) = \phi_\alpha^2 / \|\boldsymbol{\phi}\|^2$ satisfying $0 \le h_\alpha(\boldsymbol{\phi}) \le 1$ and $\sum_\alpha h_\alpha(\boldsymbol{\phi}) = 1$ for the interpolation, one can alternatively define

$$V_\alpha(\boldsymbol{\phi}) := \int_\Omega h_\alpha(\boldsymbol{\phi}(\mathbf{x}))\, \mathrm{d}\Omega. \quad (5)$$

The former definition is most in line with the interpretation of the order parameters ϕ_α being local volume fractions and has the advantage of depending solely on the phase-field values ϕ_α of the particular phase α under consideration. In contrast, the latter definition can be advantageous from a numerical point of view, as the interpolation functions are commonly chosen such that they satisfy $\partial h_\alpha / \partial\boldsymbol{\phi} = 0$ within all bulk regions, i.e. one needs not consider any derivative contributions outside the interface regions. Despite these slight differences, both approaches lead to very similar values for the phase volumes as the respective integrals are generally largely dominated by the bulk regions, such that the particular choice is primarily a matter of convenience.

2.2. Evolution equation for phase-field

In order to minimize the free energy functional in Eq. (1), the evolution equation for the phase-field is postulated following the variational approach as the gradient-flow given by

$$\epsilon\tau \frac{\partial\phi_\alpha}{\partial t} = -\left(\frac{\delta\mathcal{F}}{\delta\phi_\alpha} - \lambda\right), \quad (6)$$

with τ a time relaxation parameter and where the Lagrange multiplier

$$\lambda = \frac{1}{N} \sum_{\alpha=1}^{N} \frac{\delta\mathcal{F}}{\delta\phi_\alpha} \quad (7)$$

is added to maintain the constraint $\sum_\alpha^N \partial\phi_\alpha/\partial t = 0$. The derivative of the first contribution due to the surface energy terms in $\mathcal{F}$ [28] is given by

$$\epsilon\left(\frac{\partial a(\boldsymbol{\phi}, \nabla\boldsymbol{\phi})}{\partial\phi_\alpha} - \nabla \cdot \frac{\partial a(\boldsymbol{\phi}, \nabla\boldsymbol{\phi})}{\partial\nabla\phi_\alpha}\right) + \frac{1}{\epsilon}\frac{\partial w(\boldsymbol{\phi})}{\partial\phi_\alpha}. \quad (8)$$

For the second contribution due to the $F_\beta\left(T, V_\beta(\boldsymbol{\phi}), n_\beta\right)$, a simple application of the chain rule leads to

$$\frac{\delta}{\delta\phi_\alpha} \sum_{\beta=1}^{N} F_\beta\left(T, V_\beta(\boldsymbol{\phi}), n_\beta\right) = \sum_{\beta=1}^{N} \frac{\partial F_\beta}{\partial V_\beta}\left(T, V_\beta(\boldsymbol{\phi}), n_\beta\right) \frac{\partial V_\beta}{\partial\phi_\alpha}(\boldsymbol{\phi}), \quad (9)$$

as V_β does not depend on $\nabla\boldsymbol{\phi}$. From standard thermodynamic relations [29], the first term can be recognized as the negative thermodynamic pressure

$$P_\beta = -\left(\frac{\partial F_\beta}{\partial V_\beta}\right)_{T, n_\beta}, \quad (10)$$

whereas the differentiation of the definition of the volume $V_\beta(\boldsymbol{\phi})$ in Eq. (5) leads to the density $\frac{\partial V_\beta(\boldsymbol{\phi})}{\partial\phi_\alpha} = \frac{\partial h_\beta}{\partial\phi_\alpha}$ in the general case, with the appropriate simplification to the constant density 1 only for $\alpha = \beta$ for the simpler choice $h_\beta(\boldsymbol{\phi}) = \phi_\beta$ as in Eq. (4).

Combining both contributions, the final phase-field evolution equation is therefore given by

$$\epsilon\tau\frac{\partial\phi_\alpha}{\partial t} = -\Bigg(\underbrace{\epsilon\left(\frac{\partial a(\boldsymbol{\phi}, \nabla\boldsymbol{\phi})}{\partial\phi_\alpha} - \nabla\cdot\frac{\partial a(\boldsymbol{\phi}, \nabla\boldsymbol{\phi})}{\partial\nabla\phi_\alpha}\right) + \frac{1}{\epsilon}\frac{\partial w(\boldsymbol{\phi})}{\partial\phi_\alpha} - \sum_{\beta=1}^{N} P_\beta \frac{\partial h_\beta}{\partial\phi_\alpha}}_{rhs_\alpha} - \lambda\Bigg) \quad (11)$$

with $\lambda = 1/N \sum_{\alpha=1}^{N} rhs_\alpha$.

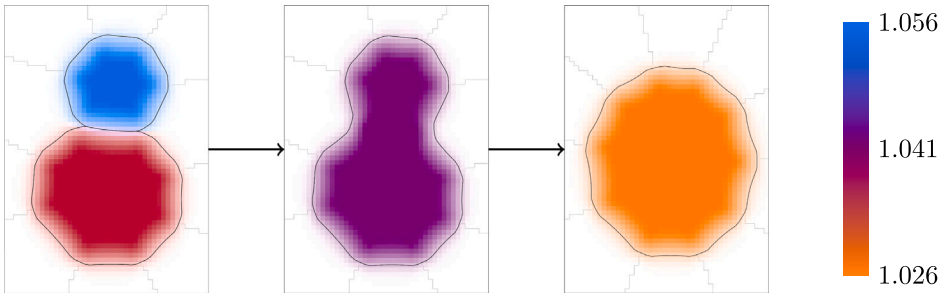

Fig. 1. Film rupture and unification of formerly separate bubbles into one, with relaxation of the structure. The algorithm ensures that the gas is treated as ideal gas and that the ideal gas law is fulfilled for unification. Colours depict different values of gas pressure.

It remains to specify the precise form of the pressure values in Eq. (11). Even though the relation Eq. (10) holds more generally, we will only consider the particularly simple case of ideal gases as it is sufficient for our purposes. Since in this case the relation $P_\alpha V_\alpha = n_\alpha RT$ holds at all times, and the phase volumes can be calculated by Eq. (5), it is sufficient either to initially specify the desired amount of substance n_α of each phase. Alternatively, one can also specify an initial pressure P_α^{init} for each phase, which, together with the initial volume of the phases, implicitly fixes the amounts of substance of each of the phases. Based upon these initial values and the current volume $V_\alpha(\boldsymbol{\phi})$, the ideal gas pressure can then always be determined using the relation

$$P_\alpha = P_\alpha^{\text{init}} \cdot \frac{V_\alpha^{\text{init}}}{V_\alpha(\boldsymbol{\phi})}. \tag{12}$$

2.3. Modelling foam evolution based on successive coalescence

By numerically solving the phase-field equations, Eq. (11), within the advanced phase-field simulation package PACE3D, we consider foam evolution. This evolution is purely based on the ageing mechanism of successive coalescence, where bursting of foam films leads to the coalescence of adjacent bubbles. Here we introduce an algorithm to describe this ageing process, assuming spontaneous, isolated film rupture. The rupture leads to the unification of two formerly separate bubbles into one (see Fig. 1), while ensuring the ideal gas law is fulfilled.

The algorithm for film bursting and coalescence is based on the selection of a foam film separating a neighbouring pair of bubbles, from all present films. For the selection, a criterion reflecting film bursting probability is evaluated in each iteration step. This selection is weighted with a random factor, which models temporal and spatial probabilistic occurrence of film rupture. The weight is in proportion to the probability of the film to rupture and the bubble pair to undergo coalescence. Upon selection of a film, respectively a pair of bubbles, the two are merged into one. This procedure mimics the mechanism of spontaneous isolated rupture of foam films.

Foam films are represented by the diffuse interface between two phases, i.e., the regions in which two phases are present. In each volume element, adjacent bubbles are defined by the two highest phase-field order parameters, ϕ_α and ϕ_β. For each volume element within the diffuse interface, a criterion is evaluated. In case the criterion is met, film bursting and the associated coalescence event is triggered. This criterion is assigned to each volume element throughout the whole simulation domain. It is represented by an expression reflecting the bursting probability in each point. The expression is a function $p_{\alpha\beta}^{\text{burst}}(\boldsymbol{\phi}, \nabla\boldsymbol{\phi}, \gamma, \ldots)$, which corresponds to a bursting probability of a single foam film, leading to the coalescence of bubble α with bubble β. We choose $p_{\alpha\beta}^{\text{burst}} = \phi_\alpha \cdot \phi_\beta$, to model a bursting criterion which is proportional to interface size, and thus to film size.

To model a spatial stochastic occurrence of rupture initiation in foam films, the probability $p_{\alpha\beta}^{\text{burst}}$ is weighted with a random uniform number z, by multiplication: $p_{\alpha\beta}^{\text{burst}} \cdot z$, $z \in [0, 1]$. Additionally, a predefined threshold value K determines an overall temporal probability for the criterion to be met. It allows for the predetermination of the occurrence of film rupture, as the magnitude of K determines the frequency. High values of K reduce overall occurrence, while low values increase it. In case the randomized probability takes a value larger than the chosen critical value,

$$p_{\alpha\beta}^{\text{burst}} \cdot z > K, \tag{13}$$

film bursting is initiated, and two adjacent initial phases are unified to form an interconnected phase with final volume, $V_{\alpha\beta} = V_\alpha + V_\beta$. This unification of two previously separate volumes is realized by summing up the two largest order parameters in each volume element, $\phi_{\alpha\beta} = \phi_\alpha(\mathbf{x}, t) + \phi_\beta(\mathbf{x}, t)$, throughout the whole simulation domain. Since only two phases are present in the diffuse interface, where the coalescence event is triggered, the former diffuse region becomes bulk. The disappearance of the diffuse interface corresponds to the foam film instantly bursting and completely vanishing. Summing up the order parameters ϕ_i leads to an interconnected volume, formed by the volumes of formerly separate bubbles,

$$V_{\alpha\beta} = \int_\Omega \left(\phi_\alpha(\mathbf{x}, t) + \phi_\beta(\mathbf{x}, t)\right) \mathrm{d}\Omega. \tag{14}$$

Upon unification, the gas pressure in the resulting phase is calculated following the ideal gas law,

$$P_{\alpha\beta} = \frac{V_\alpha P_\alpha + V_\beta P_\beta}{V_{\alpha\beta}}. \tag{15}$$

The model is implemented as part of the phase-field based multi-physics code PACE3D [26], which is in-house developed. It solves the two- or three-dimensional evolution equation on a Cartesian grid. Based on a finite differencing scheme, Eq. (11) is discretized with explicit time stepping and solved on a discrete numerical grid which is partitioned into cubic equal volume cells. Computational efficiency is achieved through using a locally reduced order parameter scheme for high number of phases [30,31]. Additionally, efficient calculation for large structures and domain decomposition is ensured by implementing parallel computing schemes to solve the evolution equations based on the message-passing interface (MPI). Subsequent sections present parallel simulations using MPI. These simulations were conducted on the high performance computing (HPC) cluster bwUniCluster (2.0).

3. Set-up

This section outlines the construction of digital models of foam structures, which serve as the basis for the numerical simulations of the decay process resulting from spontaneous film rupture, as performed within the scope of this paper. To digitally generate foam structures with a variety of morphologies, a three steps routine was applied, comprising two steps of algorithmic generation followed by a subsequent step of relaxation. Simulation snapshots of the evolution of the morphology are shown in Fig. 2. The generation routines obtain a wide spectrum of structural features, in particular various bubble size distributions. Applying the routines, we mimic the morphological and topological characteristics observed in real foam structures.

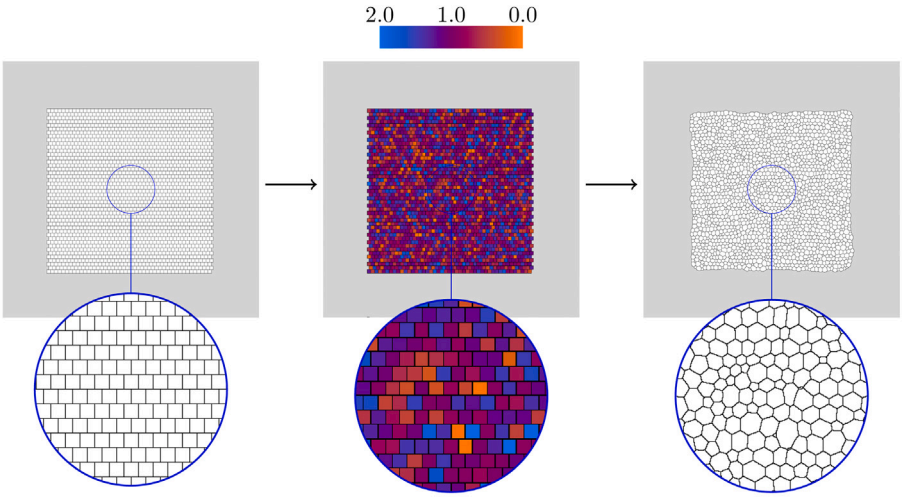

(a) Brick pattern structure; uniform sized bubbles; herein denoted as preliminary configuration.

(b) Assigned target volume factors k for equilibration process.

(c) Relaxed structure.

Fig. 2. Schematic graphic of the three steps generation routine for foam structures, with equilibration procedure: (a) Preliminary arrangement of bubble ensemble. (b) Imprinted target volume distribution assigned to bubbles. (c) Relaxed structure in energetically favourable state, through de- and increase in bubbles' volumes.

A quadratic simulation domain with quadratic cell discretization serves as base for all 2D simulation settings. The edge length of the domain is $N_x = N_y = 1400$ gridcells. The foam is represented by an initial set of $N_B = 2025$ gas bubbles.

In the first step of the generation routine (Fig. 2 (a)), the bubbles are defined as squares of 400 grid cells arranged in a brick pattern, to create a preliminary configuration. These bubbles are embedded in a liquid matrix. Each of the bubbles as well as the liquid matrix are represented by a unique order parameter ϕ_α. As the bubbles take polyhedral shape during the simulation, their size is best described by the volume, respectively the area in 2D, $V_\alpha = A_\alpha = \int_\Omega \phi_\alpha(\mathbf{x})\,\mathrm{d}\Omega$. In this work, we consider dry foam in which most of the volume is attributed to its gas phase. In this dry foam limit, foam films are negligibly small compared to the bubbles' size, and are attributed zero liquid. Furthermore, we assume that there is no liquid present in the Plateau borders, representing an idealized dry foam condition. Gas separating liquid films between two gas cells are implicitly defined by the position of the isoline $\phi_\alpha = 0.5$. The computational model represents ideal two-dimensional foams, which are distinct from real or quasi-2D foams. This idealization allows for a focused examination of fundamental foam behaviour, free from the geometric and mechanical constraints of physical experimental systems.

In the second step (Fig. 2 (b)), particular predefined distributions are imprinted on the bubble sizes, to introduce a disorder in the morphology through applying a stochastic transformation. This is facilitated by manipulating individual bubbles.

The value of target volume V of each bubble is multiplied by a factor k sampled from a normal distribution $k \sim \mathcal{N}(\mu, \sigma^2)$, $\mu = 1$, with probability density function

$$f(x) = \frac{1}{\sqrt{2\pi\sigma^2}} exp\left(-\frac{1}{2}\left(\frac{x-\mu}{\sigma}\right)^2\right),$$

considering only positive values, as a cut-off at zero is implemented to avoid negative values for V.

In the third step (Fig. 2 (c)), this generated preliminary structure has to relax into an energetically favourable equilibrium state, to form the initial setting for the decay simulations. For the relaxation step, Eq. (11) is solved numerically on a Cartesian grid. The formalism presented in Section 2 ensures the fulfilment of the ideal gas law by maintaining a constant product of pressure and target volume $P_\alpha V_\alpha$ for each individual bubble. This is achieved by considering the contribution of surface energy to the total free energy of the system, Eq. (1). Therefore, the bubbles' volumes de- or increase during the process. Thus, a polydisperse structure forms during relaxation. The free energy is plotted for the equilibration process to describe the relaxation of the structure into an energetically favourable state, see Fig. 3.

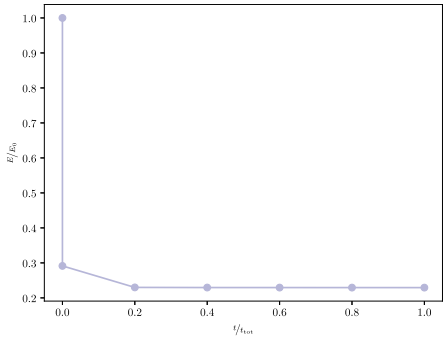

Fig. 3. Evolution of the free energy during the equilibration process, normalized values. Shown for one structure during relaxation.

For the foam decay simulations presented in Section 4, the obtained equilibrium states of foam structures are used as starting configurations. Herein, varying levels of dispersity characterize a diverse range of initial foam structures, allowing to gain insights into the impact of disorder on the structural characteristics. Configurations with different dispersities are obtained by imprinting different sets of initial values for volume to the preliminary configuration, see Table 1. For these starting configurations, normal distributions with standard deviation σ, and coefficient of variation $CV = \sigma/\mu$ are used. Upon a relaxation of the structure, the assigned target volume factors yield a disorder in bubbles' volumes, with mean volume μ_V and standard deviation σ_V. Fig. 4 illustrates the volume distribution of the bubble ensemble for the five initial configurations displayed in Fig. 5. Depending on the initial distribution of V_α, the morphology of the structures varies.

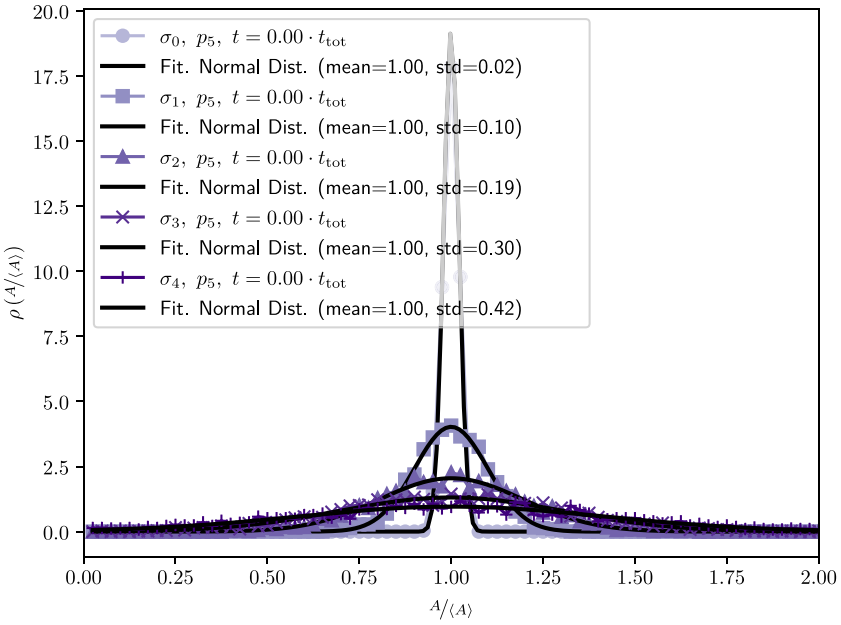

Fig. 4. Characterization of the bubble ensemble. Bubble volume distribution of different starting configurations with variation of dispersity σ_0 – σ_4. Volumes normalized by mean volume, $\langle A\rangle$.

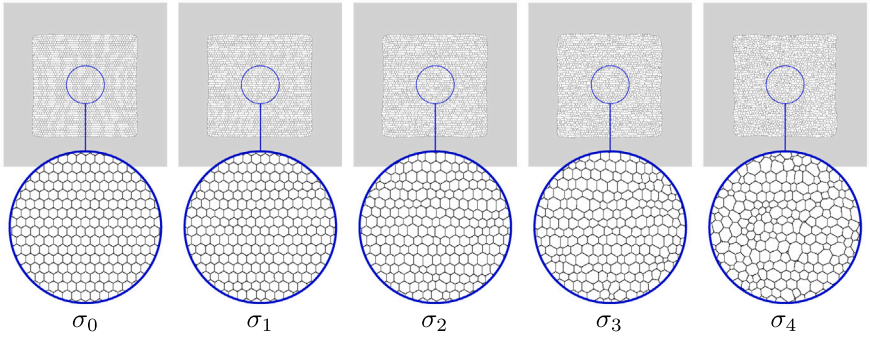

Fig. 5. Foam structures used as initial states for decay simulations, with different grades of dispersity: Structure denoted as σ_0 quasi-monodisperse, and structures denoted as σ_1 – σ_4 polydisperse with increasing degree of heterogeneity.

Table 1
Structural properties of the foams' starting configurations; values for $CV_{\text{in}} = {}^{\sigma_V}/_{\mu_V}$ are provided as input parameters, and the values obtained from analysing the equilibrated steady state relaxed bubble ensemble are mean volume μ_V and $CV_{\text{res}} = {}^{\sigma_V}/_{\mu_V}$. The differently disordered structures are denoted as listed.

CV_{in}	μ_V	σ_V	CV_{res}	denotation
0.00	382.73	7.93	0.02	σ_0
0.10	382.07	37.87	0.10	σ_1
0.20	382.90	74.52	0.19	σ_2
0.30	383.42	116.63	0.30	σ_3
0.40	372.88	154.71	0.42	σ_4

In the generated dry foam settings, variations in bubble structures become apparent with the simulation snapshots. Not only the bubbles' sizes, but also their shapes differ. This can be attributed to a higher divergence in volumes, and energy minimization relaxing into an overall favourable configuration. For disordered structures with low dispersities, the bubbles take irregular hexagonal shape. At higher dispersities, the disorder of the structure also becomes apparent, as bubbles with a lower or higher number of edges are present.

To simulate foam decay processes, eleven different stabilities of foam films are modelled by choosing the bursting probability of a volume element of a film Eq. (13), herein denoted as $p_i, i = 0, \ldots, 10$. These stabilities are applied to the five starting configurations, denoted as in Tables 1 and 5, i.e. a total of 55 different foam decay processes are simulated, as sketched in Fig. 6. By this varying of foam film stability, different foam decay velocities are modelled. For the dynamical evolution of the foam during the decay process, Eq. (11) is solved. This leads to temporal, incomplete relaxation towards energetic minima. The relaxation is interrupted by the triggered bursting of foam films followed by coalescence of bubbles, which introduces local perturbations of the relaxation. In between coalescence events, the structure evolves, driven by relaxation into another energy minimum. Throughout the dynamical simulation, equilibrated states are almost never reached. Fig. 7 shows the energy during the decay process, i.e. the dynamical evolution of the foam with bursting films.

4. Results

In this section, we highlight the primary capabilities of our numerical approach. This comprises an overview of the predictive capabilities accessible through numerical simulations, and the validation of our microstructure evolution model. The method, implemented within the software package PACE3D, is designed to capture the microstructural evolution of decaying foam governed by film rupture and coalescence events. It finds application in the systematic exploration of diverse foam geometries via comprehensive parameter studies. This demonstrates

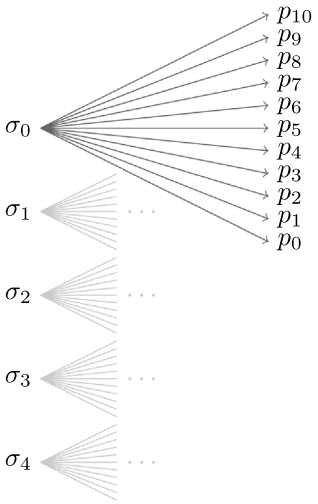

Fig. 6. Sketch of the complete set of decay simulations performed within the study. Starting from five differently dispersed structures, denoted $\sigma_0 - \sigma_4$, decay simulations are run for 11 different foam film stabilities, $p_0 - p_{10}$.

a large versatility by enabling access to a broad range of structural attributes. Thereby, it reveals the potential and possibilities that simulations and evaluations can offer in understanding complex foam phenomena. While a detailed introduction of the numerical method is provided in Section 2, we offer a contextual summary here to underline the relevance to the findings presented in this section.

The essence of our studies lies in the introduction and validation of our microstructure evolution model, via numerical simulations. By employing a phase-field method, we enable to represent the foam's dynamic evolution, while incorporating the spontaneous rupture of foam separating films and the coalescence of bubbles. Our study enables access to four key points regarding a refined foam representation. First, the method inherently accounts for the gas pressure within the bubbles, contributing to a detailed representation of a foam. Second, our routines facilitate the digital generation of diverse foam structures, each characterized by unique morphological attributes and varying degrees of order in bubble dimensions. Third, the model's versatility comprises variable film bursting probability, mimicking variable degree of decay rate. The film rupture events drive structural changes, contributing to the dynamic nature of microstructure evolution. Fourth, our approach is proficient in determining the complex morphological and topological characteristics inherent in foam structures. By digitally creating foam structures and subjecting them to decay simulations specifically driven by spontaneously rupturing films, we gain insight into the impact of geometry and bursting probability of individual films on the overall foam structure.

The method's adaptability to simulating ensembles of several thousand bubbles allows exploring statistical properties of foams based on bubble-scale characteristics. This connection is strengthened by empirical data derived from the simulations, which distinctly show the logical coherence and validity of our model. An advantage of our numerical approach is the suitability for large-scale microstructure simulations. The ability to simulate large foam domains gives access to patterns that emerge from the collective behaviour of individual bubbles, and is particularly valuable for examining statistical properties of foams. The empirical results obtained from our numerical experiments offer both visual and quantitative insights into the temporal evolution of foam decay. Statistical analysis deepens our understanding of how microstructural parameters are interconnected. We focus on diverse parameters for the microstructure characterization; bubbles' volume, pressure, shape in terms of edges, and neighbouring relationships. This investigation serves a dual purpose: It enables the comprehensive evaluation of the model's predictive capability, and describes the boundaries of its applicability.

The subsequent section explores microstructure evolution, guided by statistical analysis. The probabilistic dynamics of decay influence the interplay of various parameters. Through the effective integration of film rupture, our framework provides a platform for gaining insight into the complex behaviour of decaying liquid foams. The central achievement facilitated by the proposed microstructure evolution model is in connecting the stochastic occurrence of film ruptures with empirical observations of the overall bubble ensemble. This is tested for a set of foams with various morphological parameters in simulated decay experiments.

4.1. Validation: Single bubble equilibrium state

In order to validate the method described in Section 2, we present results of numerical simulations of a bubble within a liquid and assess the method's capability to accurately predict the gas pressure in the equilibrated state. The simulation setup for the validation consists of an incompressible liquid matrix with an embedded compressible gas bubble, assuming an ideal gas. For initializing the simulations, a set of configurations is generated and tested on a domain discretized into quadratic cells, and $\epsilon = 3$. Herein, the bubble is initially defined as a phase described by the order parameter ϕ_α, the liquid by ϕ_β. Variations of both the initial radius of the bubble r_0, and the surface energy $\gamma_{\alpha\beta}$ were systematically selected to cover a representative parameter space and capture the method's applicability to various scenarios. The system was relaxed into an energetic minimum state through surface minimization. This equilibration process allows the system to reach a stable state, characterized by a balance between the resulting forces due to gas pressure and surface tension. On the equilibrated configuration, we obtain the numerically calculated gas pressure of the bubble $P_{\text{eq.}}$ and the pressure of the liquid matrix P_0 as inherent to the methodology. For the set of simulations, the pressure of the liquid takes constant values of $P_0 = 1$. The pressure difference between bubble and matrix $\Delta P = P_{\text{eq.}} - P_0$ serves as a fundamental metric for validating the accuracy of our method. These computed pressure differences are compared with the analytical solution provided by Young–Laplace equation. The theoretical pressure difference is given by

$$\Delta P = \frac{\gamma_{\alpha\beta}}{r_{\text{eq.}}} (d - 1), \tag{16}$$

for $d \in \{2, 3\}$ dimensions. Fig. 8 provides a comparison of the computed pressure difference and the theoretical values for a two-dimensional setup. The validation results demonstrate agreement between computed and theoretical pressure differences across various bubble volumes and surface energies. Minor discrepancies observed for large reciprocal radii can be attributed to the numerical resolution. Overall, the results validate the method's reliability for simulating bubble behaviour as an ideal gas in liquid matrices. To guarantee stability of the method applied to foams, bubble sizes for the studies presented within this paper are chosen within a reasonable range.

4.2. Microstructure evolution in the dry foam limit

In this section, we present an analysis of the microstructural evolution of decaying foam structures in the dry foam limit, comprising a visual representation of the simulation studies and statistical characterization. We initiate our examination by visually documenting the dynamic evolution of foam structures during the decay process, as exemplarily shown in Fig. 9 for a moderately disordered starting morphology with dispersity σ_2 imposing an intermediate film bursting probability p_5. Through morphological observations, we track the overall evolution of the bubble ensemble over time. This visual assessment forms the basis for capturing the transformations underlying

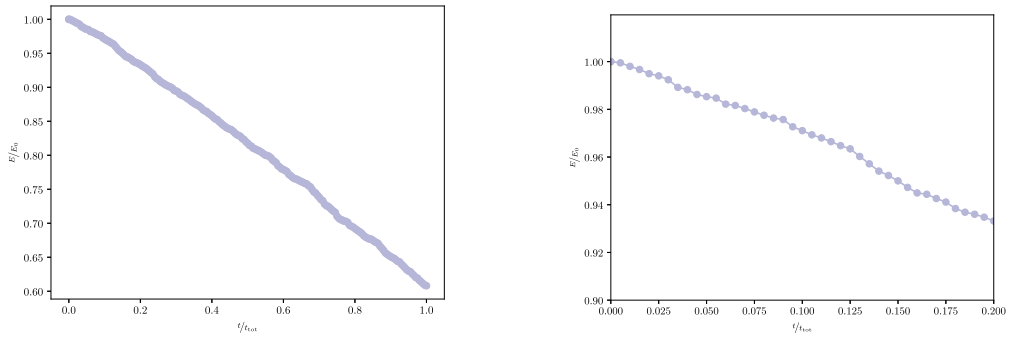

(a) Free energy versus time.

(b) Detail zoom of (a).

Fig. 7. Evolution of the free energy during the decay process, exemplarily shown for structure σ_2, film bursting probability p_5 (intermediate).

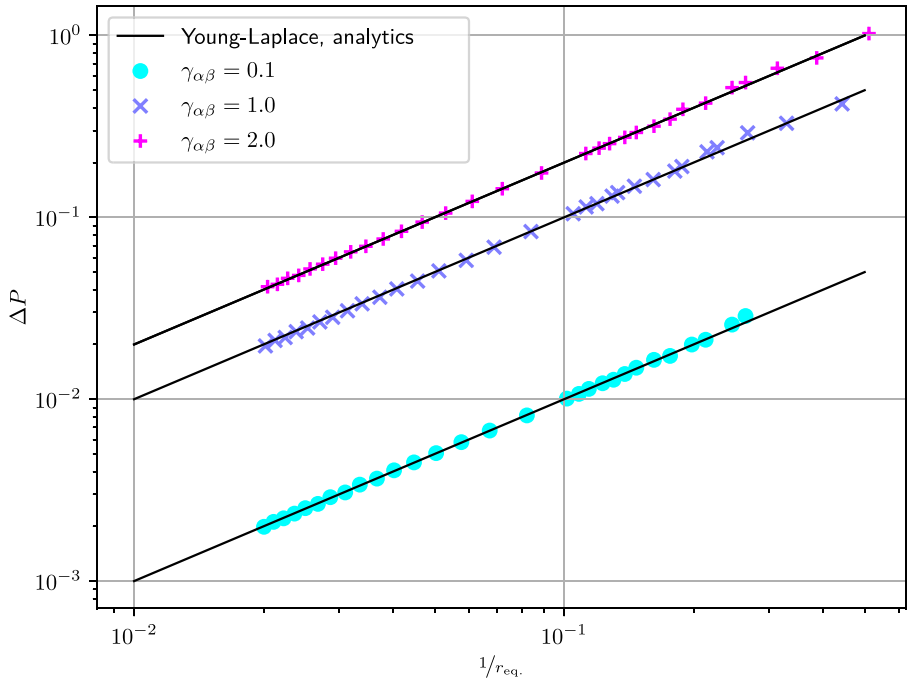

Fig. 8. Pressure difference ΔP as function of reciprocal radius $r_{\mathrm{eq.}}$ of a bubble embedded in a liquid matrix, in equilibrium. Data presented for three different values of surface energy $\gamma_{\alpha\beta}$, for a two-dimensional setup. The black line represents the solution obtained from the theoretical Young–Laplace equation.

foam decay. Varying microstructural and physical parameters influence the structure formation both in static and dynamical settings. The investigation of film bursting probability variations shows distinctive changes in the foam's morphology over time. This study was conducted on a consistent initial setup. The temporal progressions corresponding to three distinct film bursting probabilities are graphically represented in Fig. 10. Differences in bubble sizes, and pattern formation, become apparent for different decay rates. The morphological alterations are as well accessible through experimental observations. To investigate the impact of this variation on foam decay dynamics, we explored a range of bursting probabilities.

At notably high bursting probabilities, the formation of unconventional bubble shapes occurs. In contrast, lower bursting probabilities facilitate a gradual evolution, enabling relaxation of the foam structure. This contrast underlines the interplay between bursting probability and the unfolding dynamics of foam evolution. The bursting probability can be chosen as variable, and therefore facilitates the calibration of decay rate. Investigation of the decay process for varying initial configurations (different dispersity) tested for equal film bursting probabilities show their influence on foam morphology, see Fig. 11. Throughout the simulated decay process for the chosen structures, minor visual differences can be seen. Within the tested set, varying starting configurations and dispersity appear to have a limited impact on the morphological evolution.

For structures with larger dispersity, the film length is more inhomogeneous. The probabilistic nature of film bursting is connected with film length. Films of differing lengths exhibit varying probabilities of bursting. The variation in film length corresponds to varying probability of bursting for the overall film. This relationship highlights the significance of film length as a critical factor in determining the dynamic behaviour and evolution of the foam.

4.3. Statistical characterization of microstructural parameters

Based on the visual analysis, we look at the microstructural parameters in greater detail through a statistical investigation, to understand the foam's internal structure and its dynamic tendencies. The following attributes characterize the structure, each of which responds distinctly to variations in film bursting probabilities and starting configurations: The bubbles' volume, gas pressure, shape, and neighbour relations. Therefore, the focus on the essential attributes guide our investigations. Furthermore, the statistical approach facilitates to extract trends and characteristic curves, systematically exploring the temporal evolution.

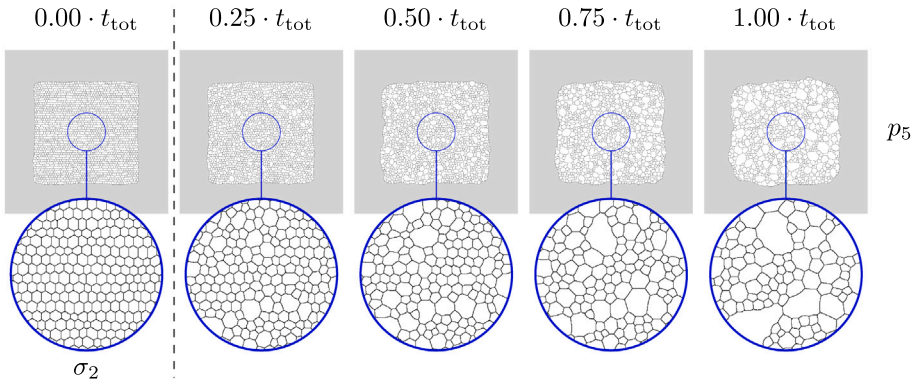

Fig. 9. Series of simulation snapshots showing the evolution of the bubble ensemble over time. Morphology of bubble ensemble is shown for moderately disordered starting morphology with dispersity σ_2, intermediate film bursting probability p_5.

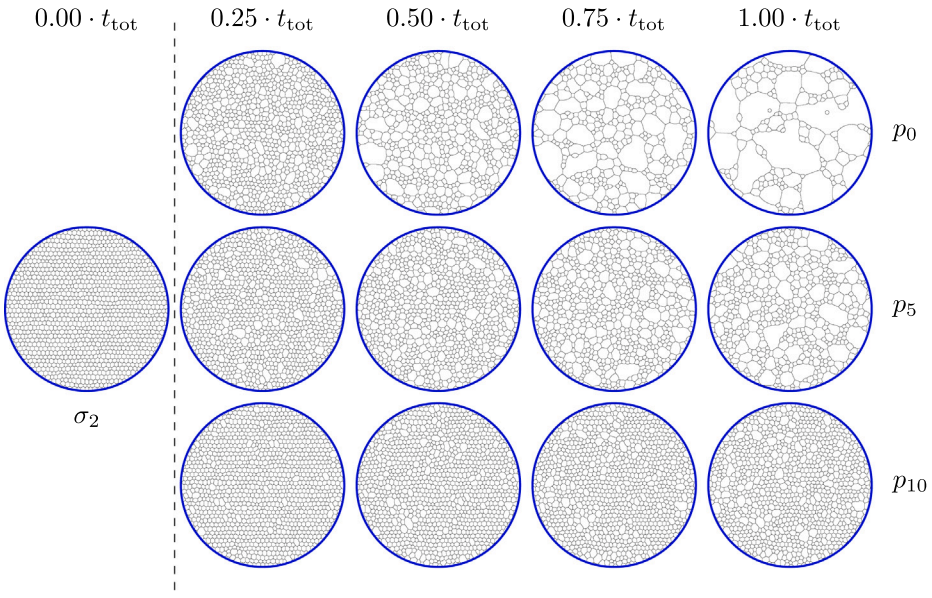

Fig. 10. Series of simulation snapshots showing the evolution of the bubble ensemble over time. Morphology of bubble ensemble is shown for starting morphology σ_2. Three different film bursting probabilities, p_0 high, p_5 intermediate and p_{10} low probability.

4.3.1. Decay dynamics of evolving foam

Statistical analysis reveals the temporal trends in the formation of the bubble ensemble, quantified by the number of bubbles, and allows to identify the influence of varying film bursting probability and disorder in foam structure. The temporal evolution of the number of bubbles serves as measure for the decay rate. Fig. 12 depicts the time dependent number of bubbles during the decay simulation for structure σ_2. The number of bubbles is found to decrease monotonically over time, with varying slope for different probabilities; the higher the probability, the faster the reduction. The trend is not linear, indicating a faster reduction in the number of bubbles associated with faster decay at the beginning of the process. A similar behaviour is observed for structures with differently dispersed starting configurations. The individual trajectories vary due to the probabilistic nature of the algorithm and the presence of differently disordered configurations which are reached throughout the simulation. Over the course of the decay simulation, the influence of the initial configuration becomes evident with the evolution of the number of bubbles, see Fig. 13. Among structures with different degrees of initial order, the decay rate notably varies, although the probability of film rupture per volume element remains constant. Within the set chosen for our simulations, in highly disordered structures, a greater number of bubbles persists for a longer duration. In comparison, for structures with smaller degrees of disorder, only marginal differences exist, and the impact of the degree of disorder is not measurable. Therefore, evaluating additional meaningful parameters is beneficial, as they may show more distinct variations in influence.

4.3.2. Bubble volume and distribution

Statistical analysis of bubble volumes quantifies the morphology, assessing the foam's microstructure. By analysing volume distributions and mean values, the impact of bursting probabilities and initial configurations on foam structure becomes evident. An integral aspect of the analysis contains the temporal evolution of the mean bubble volume, obtained as $\langle A \rangle = \frac{1}{N(t)} \sum_{\alpha=1}^{N(t)} A_\alpha$, with $N(t)$ denoting the number of bubbles present at time t. The evolution shown in Fig. 14 exhibits distinct characteristics based on the bursting probability variations. The mean bubble volume increases over time, with a more pronounced steepness in cases of higher bursting probability. As the decay process advances, a progressively greater increase in the mean bubble volume becomes evident. For a detailed analysis of the volumes of the bubbles during distinct times of the decay process, we examine the temporal evolution of the probability distribution of volume of the bubble ensemble, as illustrated in Fig. 15. Throughout the progression,

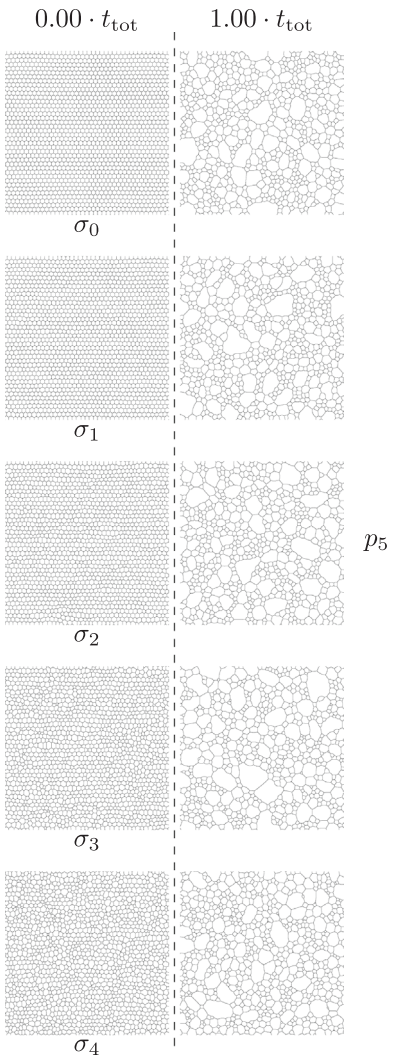

Fig. 11. Evolution of the bubble ensemble over time. Morphology of bubble ensemble is shown for variation of the starting dispersity, for equal intermediate bursting probability of p_5. Snapshots show starting configurations (first column) and configurations at end of simulation (second column).

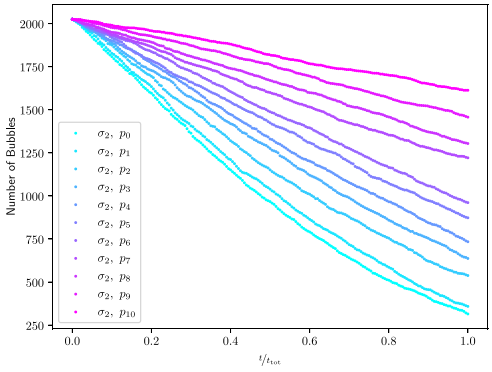

Fig. 12. Evolution of the bubble ensemble over time. Time dependent number of bubbles is shown under parametric variation of the film bursting probability p_n, exemplarily for starting configuration σ_2.

not only the mean volume of the bubble ensemble increases, but further trends become evident. The distribution of individual values of absolute volumes, Fig. 15, gradually flattens and broadens over time,

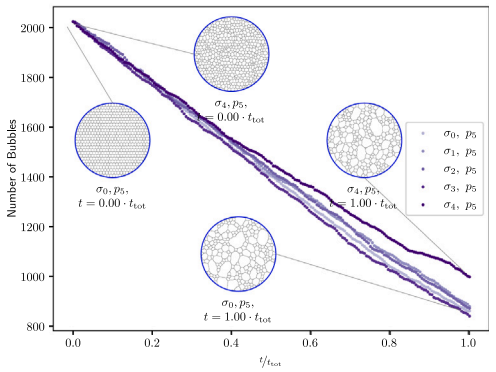

Fig. 13. Evolution of differently dispersed initial structures for equal intermediate bursting probability p_5, leading to distinguishable decay rate.

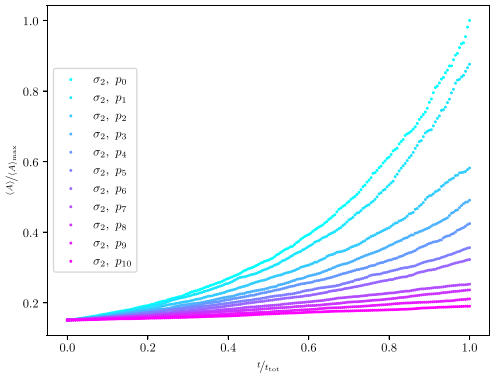

Fig. 14. Evolution of the bubble ensemble over time. Time dependent mean bubble volumes of ensembles are shown under parametric variation of the film bursting probability p_n, for starting structure σ_2. Mean volume is normalized by maximum mean volume.

reflecting changes in the morphology. The number of bubbles with larger volumes tends to increase, due to the continuous rupture of films and coalescence, leading to the expansion of their sizes. Peaks tend to congregate at integral multiples of the initial volume. This observed doubling of volumes is associated with bubble coalescence events. Additionally, we employ the bubble volume normalized by the average volume in Fig. 14, as it offers a standardized metric to assess bubble size variations within the foam ensemble. This normalization allows us to better discern trends in the distribution's shape, related with bubble growth. Regarding this distribution, the peaks of the volume distribution gradually shift towards smaller values, as expected for an evolving foam. Thus, this shift indicates an overall broadening of bubble sizes towards larger values. Further analysis of the bubble size distribution at distinct time complements the understanding of foam dynamics in response to varying bursting probabilities. Significant divergence shows in the bubble volume distribution at different distinct time steps, for foams with different film stability. Fig. 16 illustrates volume distributions in comparison, for the same starting configuration of σ_4, and Fig. 17 compares the evolution for the starting configuration of σ_2. The distributions of bubble volumes at a distinct time differ, depending on the bursting probability. The development over time, recorded in the panels in fixed time steps, shows that the peaks diverge and flatten out differently depending on the film bursting probability. Bubble ensembles with higher bursting probability feature increased mean volumes, compared to lower bursting probability. In the distribution, higher bursting probably is associated with a shift of the peak towards smaller values. This underlines the sensitivity of the foam structure to varying probabilities of film bursting.

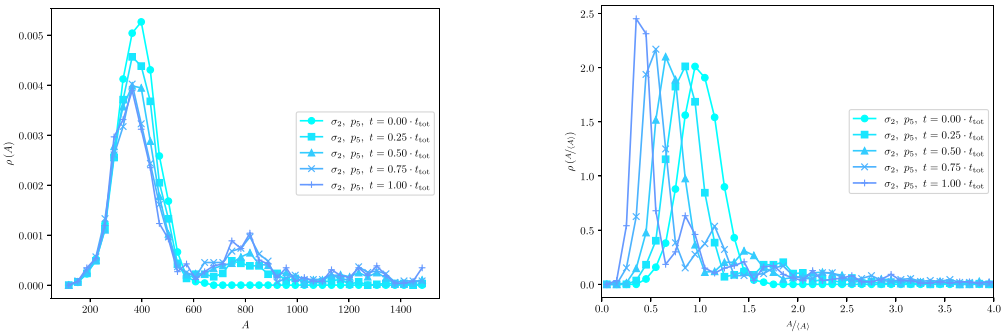

Fig. 15. Evolution of the bubbles' volumes for the initial structure σ_2 evolving under intermediate film bursting probability, p_5. Ensemble characterized for different time steps during evolution, shown absolute values of volume A, and normalized by mean volume, $A/\langle A\rangle$.

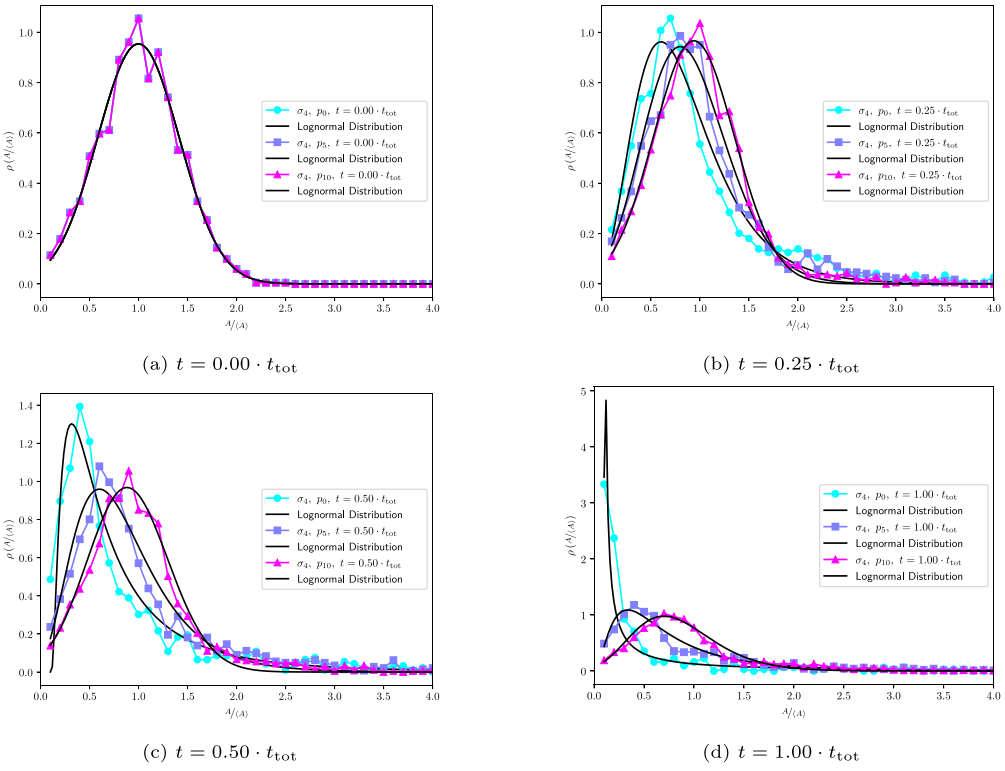

(a) $t = 0.00 \cdot t_{\mathrm{tot}}$ (b) $t = 0.25 \cdot t_{\mathrm{tot}}$

(c) $t = 0.50 \cdot t_{\mathrm{tot}}$ (d) $t = 1.00 \cdot t_{\mathrm{tot}}$

Fig. 16. Comparison of volume distributions for constant starting dispersity of heterogeneous structure σ_4 for three different bursting probabilities, high p_0, intermediate p_5, low p_{10}. Panels (a) – (d) show probability density of normalized bubble volume, $A/\langle A\rangle$, at four different distinct times. Log-normal fit is included as guide to the eye.

Comparing the decay for different initial configurations, its influence on the mean bubble volume is analysed for the specific film bursting probability of p_5, see Fig. 18. For all investigated structures, the evolution seems largely similar, indicating a rise for all structures with time. In the case of the starting configuration with the highest dispersity σ_4, a distinction is noticeable. The mean bubble volume exhibits lower values, and evolves with a slower slope. For the other, lower dispersity configurations, our simulation does not reveal any discernible influence on the evolution of bubble volumes. This discrepancy underscores the sensitivity of the system to initial conditions for comparably high degrees of disorder in the initial setting, as the highly disordered starting configuration impacts the subsequent dynamics of the bubble ensemble, while for lower dispersity configurations this appears to have negligible effects. For a detailed analysis of bubble volumes for structures with variable degree of disorder, Fig. 19 gives an overview over the volume distributions for different distinct time steps. Structures with low dispersity yield prominent peaks at integer multiples of the initial mean volume, Fig. 4, whereas structures with moderately and high dispersity show smearing of these peaks. In low dispersity structures, where bubble sizes are uniform, a film bursting event often doubles the resulting bubble's volume. Conversely, in highly dispersed structures with varying bubble sizes, the resulting volume increase is less predictable, as heterogeneous sizes contribute differently to the resulting volume. This highlights the influence of dispersity on structural characteristics, and reveals the interplay between disorder and organization during the evolution.

4.3.3. *Gas pressure and pressure field*

Investigation of the gas pressure within the bubbles provides insight into the degree of order characteristics of the evolving foam. Simulation results give access to pressure variations of individual bubbles and the overall evolving foam. The methodology presented in Section 2 has the central feature to calculate gas pressure within individual bubbles at each time step, considering ideal gas behaviour. This pressure is consistently updated throughout the simulation, yielding a pressure field that spans the entire bubble ensemble. The method enables a straightforward insight into the pressure of individual bubbles of the ensemble, without the need for complex additional calculation methods. Note that

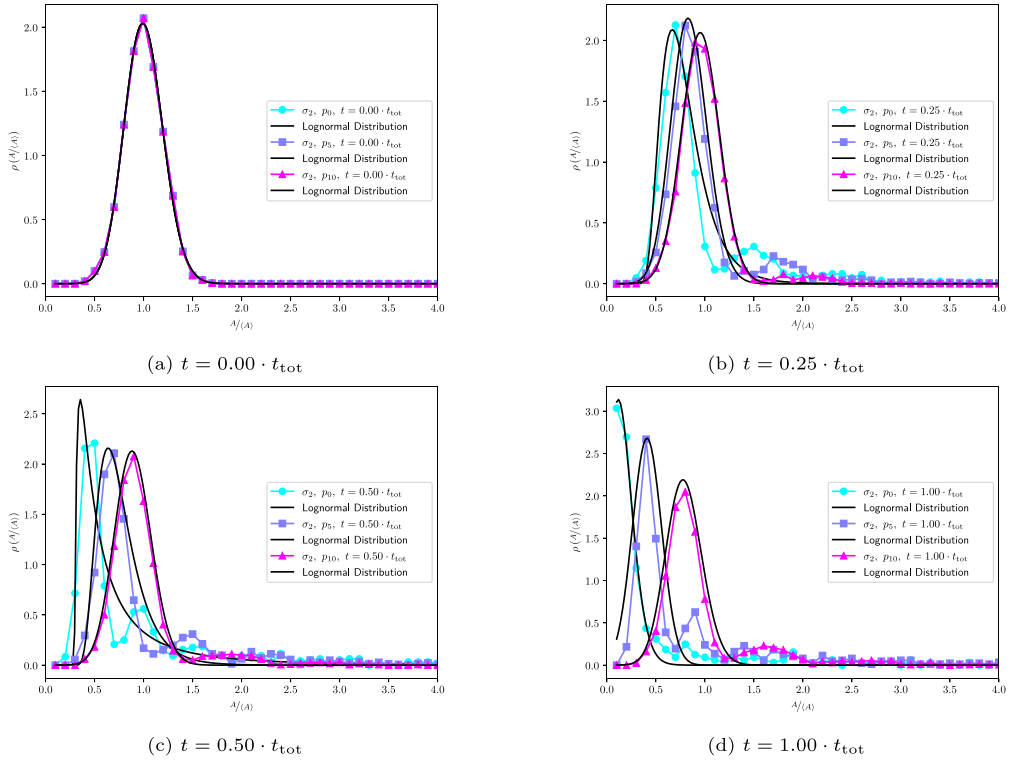

(a) $t = 0.00 \cdot t_{tot}$ (b) $t = 0.25 \cdot t_{tot}$

(c) $t = 0.50 \cdot t_{tot}$ (d) $t = 1.00 \cdot t_{tot}$

Fig. 17. Comparison of volume distributions for constant starting dispersity of slightly disordered structure σ_2 for three different bursting probabilities, high p_0, intermediate p_5, low p_{10}. Panels (a) – (d) show probability density of normalized bubble volume, $A/\langle A \rangle$, at four different distinct times. Log-normal fit is included as guide to the eye.

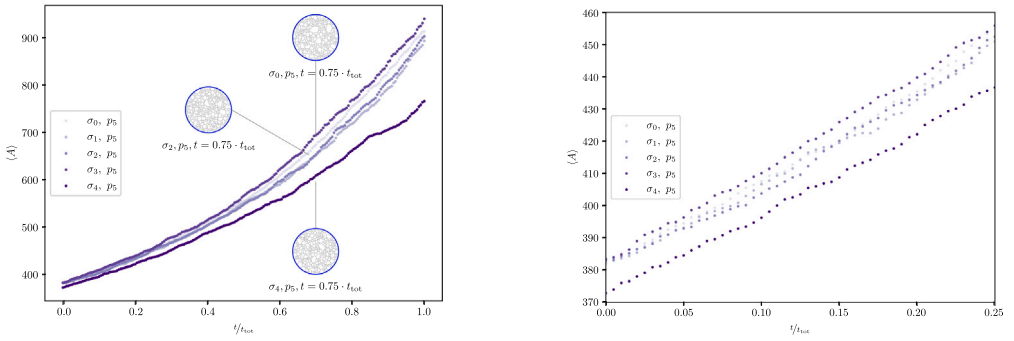

(a) Complete time series. (b) Detail from panel (a).

Fig. 18. Evolution of the bubble ensemble over time. Time dependent mean volume of bubbles $\langle A \rangle$ is shown for five different variations of starting configuration with dispersities, σ_0 - σ_4, the film bursting probability is intermediate, p_5.

after initializing the simulation with an imprinted pressure distribution, the structure equilibrates, see Section 3. During the course of the decay simulation, the method ensures pressure values following ideal gas law. In Fig. 20, analysis of gas pressure for the exemplary structure σ_2 with varied bursting probability is shown. Throughout the simulation, mean bubble pressure remains nearly constant, which is inherent to the method. However, minor variations can be observed during the temporal course in Fig. 20(a). These are likely to emerge from local perturbations through film rupture, and subsequent rearrangement and relaxation in local energy minima. The slight overall decrease associated with high and intermediate bursting probability reflects the bubble ensemble tending towards spherical shape, and therefore optimum shape associated with energetic minimum. For low bursting probability, this decrease is not visible in the analysed simulation span. In Fig. 20(b), the standard deviation of average gas pressures within foam bubbles demonstrates a strong increase over the observed time span. This substantial variation in standard deviation becomes apparent, while the measured absolute values of average gas pressures remain within a narrow range throughout the entire duration of the study. The increase in the width of the distribution of gas pressures suggests a growing level of heterogeneity in the pressure distribution among the bubbles over time. It implies that while the average pressure remains relatively stable, the dispersion of individual pressure values among the bubbles is becoming more pronounced, emerging from the underlying dynamics and structure formation within the foam. The strongest increase is recorded for the evolution under highest bursting probability, with a fourfold increase. Less pronounced increase is observed for the evolution with smaller film bursting probabilities. Fig. 21 depicts the temporal evolution for differently ordered initial structures with equal bursting probability. These structures exhibit similar characteristics over time, marked by a slight initial increase followed by an overall decrease in pressure. Notably, the structure

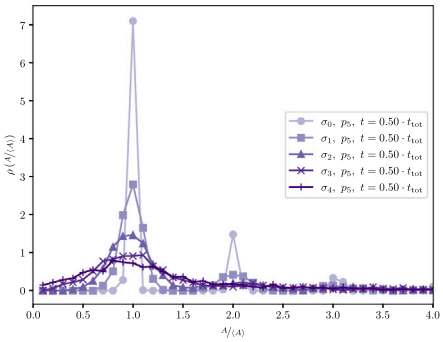

(a) $t = 0.50 \cdot t_{\mathrm{tot}}$, volumes normalized by mean volume, $\langle A \rangle$.

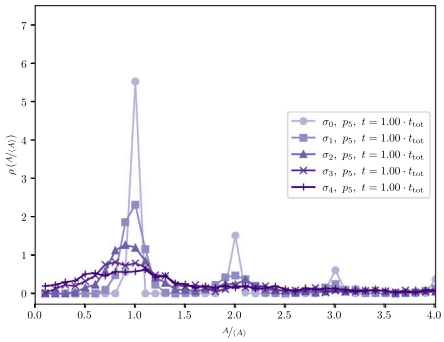

(b) $t = 1.00 \cdot t_{\mathrm{tot}}$, volumes normalized by mean volume, $\langle A \rangle$.

Fig. 19. Characterization of the bubble ensemble. Bubble volume distribution of different starting configurations with variation of dispersity σ_0 – σ_4, with fixed intermediate bursting probability p_5. Analysis of bubble volume for two different distinct time steps during the evolution.

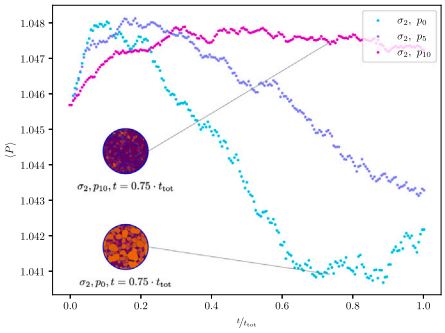

(a) Mean gas pressure.

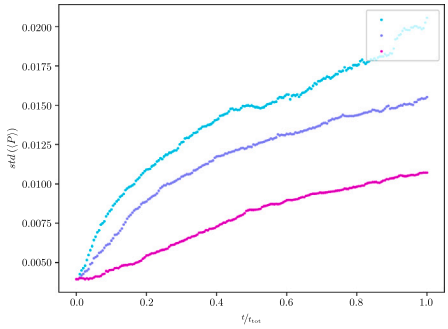

(b) Standard deviation of a).

Fig. 20. Temporal evolution of bubbles' gas pressure. Ensemble values for foam structure σ_2, variable film bursting probability.

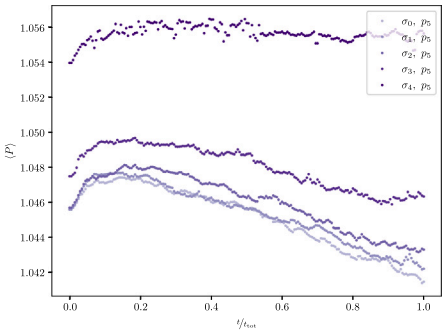

(a) Mean gas pressure.

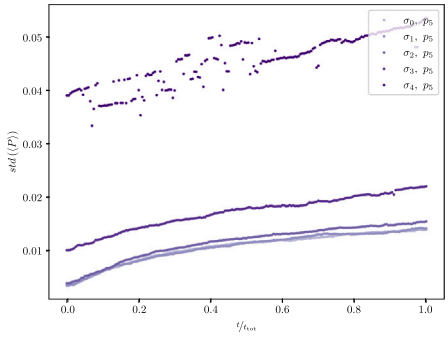

(b) Standard deviation of a).

Fig. 21. Temporal evolution of bubbles' gas pressure. Ensemble values for foam structures with different degree of order.

with the highest disorder, represented by σ_4, demonstrates the least smooth evolution. The presence of pressure jumps in this structure can be attributed to the coalescence of pairs consisting of large and small bubbles, followed by more substantial relaxation dynamics.

The standard deviation, as depicted in Fig. 21(b), portrays the temporal evolution of differently ordered initial structures, all with equal bursting probability. In the case of low initial dispersity, there is a smooth course and slight increase in standard deviation over time, indicating relatively consistent pressure values among bubbles within these ordered structures. Conversely, for high initial dispersity, the standard deviations initially exhibit higher values, reflecting substantial variability in pressure distribution among bubbles. These variations are likely to emerge in time steps where one or more bursting and coalescence events happened, and the structure has not yet relaxed towards a local minimum energy state. However, as time progresses, these variations tend to stabilize, indicating a convergence towards a more consistent pressure distribution within the foam structure. Besides considering ensemble values, the variation of pressure inside the ensemble is of particular interest. Our method allows for precise analysis of the individual bubbles' pressures. For five distinct time steps, a detailed analysis of bubbles' gas pressure distributions is shown in Fig. 22. The evolving structure features an almost symmetric distribution of pressure values at the beginning of the decay process, whereas throughout the temporal course, the distribution becomes more asymmetric. Besides the general broadening and flattening of the distribution, bubbles with smaller magnitude of pressure become more prevalent. This development of the ensemble is in accordance with the development in volumes analysed in Fig. 15, where the number of

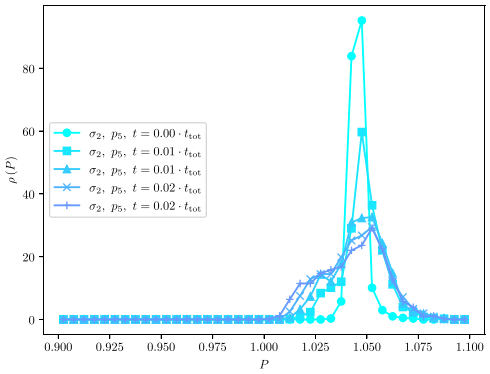

Fig. 22. Distribution of bubbles' gas pressure at distinct times of the foam evolution.

larger bubbles is observed to grow, as ideal gas law ensures a constant product $P \cdot V$ for each bubble.

Fig. 23(a) shows the pressure distribution for the ensemble for the starting configuration σ_2 for three different bursting probabilities, at the distinct time of $t = 1.00 \cdot t_{\mathrm{tot}}$. For low bursting probability, p_{10}, the distribution remains mostly symmetric, and shows only slight asymmetry for smaller values. Here, a relatively small amount of films have burst. For high bursting probability p_0, we observe the most pronounced deviation from the initially predominantly symmetric distribution, with the majority of values skewed towards lower values. With more burst foam films, the amount of bubbles with higher volume increases, and therefore the associated shift towards lower values of pressure occurs. To further characterize the variations among differently dispersed structures, Fig. 23(b) illustrates the pressure distribution at $t = 1.00 \cdot t_{\mathrm{tot}}$ for intermediate bursting probability p_5. Minor deviations in the distributions become apparent. In the case of the more ordered structures characterized by low initial dispersity, the distribution exhibits primarily symmetrical characteristics, with a slight skewness towards lower values. With increasing dispersity, we observe a more pronounced flattening and broadening of the distribution. Consequently, more bubbles with higher gas pressure values are prevalent. This illustrates that the influence of the initial dispersity remains discernible throughout the entire simulation. Initially, a wider range of volumes and, consequently, gas pressures exists, thereby exerting a lasting impact on the simulation dynamics.

4.3.4. Bubble shape

Statistical characterization of bubble shapes, specifically characterized by the attribute of number of edges, offers a comprehensive view of the changing foam geometry. This analysis facilitates an understanding of how local topology on the scale of single bubbles is connected with overall structure, depending on varying parameters. For the foams in the dry foam limit we investigate, the bubbles are densely packed and in contact with each other. The number of edges is obtained through the number of direct neighbours.

Fig. 24 illustrates the temporal course of the evolution for one starting configuration under three different bursting probabilities. In each of the three investigated decay processes, the mean number of edges of a single bubble shifts towards smaller values as the foam evolves. For foam with low bursting probability, the evolution is slow and therefore the number changes only slightly, whereas for high bursting probability p_0, a dominant decrease can be observed. Note that the values for mean edge number are slightly lowered due to bubbles at the corner of the cluster contributing to the calculation of the mean, which naturally have less neighbouring bubbles, and therefore edges. Additionally, we explored the number of edges each bubble has depending on initial dispersity, see Fig. 25. At early stages of the evolution, bubbles in the relatively high disordered structure σ_4 tend to have fewer edges than the ones in comparably less disordered structures. Conversely, at later stages of the evolution, the foams tend to show increasingly similar behaviour. Differences in mean edge number for the different structures become less evident. This behaviour is also underlined by the temporal evolution of the width of the distribution, see Fig. 25(b). Whereas at low evolution times the structures feature clearly distinguishable standard deviations for the differently dispersed settings, they tend to align and get less distinguishable at later times. Foam dispersity only has a minor effect in terms of bubbles' edges in the investigated set. The edge distribution for distinct time steps during the evolution are plotted in Fig. 26, for the starting configuration σ_2 evolving under three different bursting probabilities. As expected for an evolving foam with intermediate initial structural disorder, most bubbles have six edges at the start, with a narrow distribution. The peaks of the edge distribution show a transition and shift towards smaller values with time. Here we observe $\rho\left(N_{\mathrm{E}}\right)$ increasing for $N_{\mathrm{E}} < 5$, and decreasing for $N_{\mathrm{E}} > 5$. Bubbles with five edges, $N_{\mathrm{E}} = 5$, show somewhat different behaviour, with a rise, followed by a reduction. Eventually, the four-sided bubbles are dominant. Bubbles with a large number of edges, $N_{\mathrm{E}} > 8$ are not considered in the interpretation for low statistical prevalence. With high bursting probability, the transition shows as most pronounced, tending towards the most smooth distribution. Fig. 26(d) presents the data for the starting configuration σ_4 as one representative for a structure with higher degree of disorder. In comparison with Fig. 26(b), the effect of the initial structure on the overall distribution during the temporal evolution can be a certain influence.

Fig. 27 illustrates the temporal evolution of number of edges, for $3 \leq N_{\mathrm{E}} \leq 8$ in two differently dispersed initial structures, both at equal intermediate bursting probability. This data describes the probability of a randomly chosen bubble having N_{E} edges. Regarding the temporal course for structure σ_2, Fig. 27(a), the initial predominance of bubbles

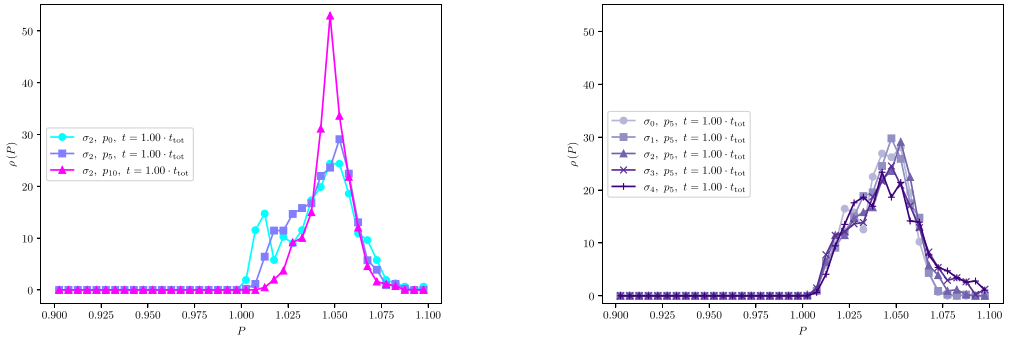

(a) Gas pressure distribution for variable bursting probabilities.

(b) Gas pressure distribution for variable foam dispersities.

Fig. 23. Analysis of bubbles' gas pressure for different focus, at distinct time steps of the evolution.

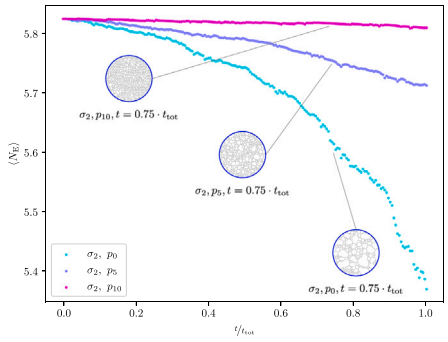

Fig. 24. Temporal evolution of mean number of bubble edges, for one starting dispersity and three different bursting probabilities.

with six edges is gradually surpassed by those with five edges. At advanced times, bubbles with four edges also become increasingly prevalent. For both bubbles with five and six edges, initially there is a steeper de- and increase in the probability, which later levels off. However, an opposite pattern emerges for bubbles with four edges. Comparing with the data obtained for structure σ_4, Fig. 27(b), the findings indicate that these shifts in the predominant number of edges occur at different times. Furthermore, the temporal evolution of edge counts displays relatively smooth trends for the more ordered structure compared to the variations observed for structure σ_4. These variations suggest that higher initial dispersity induces more pronounced relaxation events.

4.3.5. *Connectivity and distances to neighbouring bubbles*

Exploring foam complexity extends beyond evaluating the number of edges of individual bubbles. Also, understanding the connectivity of individual bubbles is crucial in many foam applications. Our framework facilitates to conveniently access the barycentre of each bubble and establishes bubble interconnections, assessing foam homogeneity. To determine the homogeneity of a foam structure, the dispersity in bubbles' volumes is often considered, or the film length is investigated to characterize foams. Additionally, here we introduce the distance between barycentres of neighbouring bubbles as a more comprehensive measure of foam complexity. This metric assesses an additional measure of foam disorder.

We analysed the mean distance of all neighbouring bubbles to each individual bubble, $\langle D \rangle$, for the simulation runs under variation of bursting probability. Fig. 28 illustrates the temporal course. The evolution qualitatively aligns with the trends observed for the evolution of bubbles' volumes, as shown in Fig. 14, as a relationship over the square root is presumed. The comparison for structures with varying starting dispersity is depicted in Fig. 29. In all cases, the mean distance of barycentres increases as the decay progresses. These findings are consistent with previous observations made regarding the temporal evolution of volumes. However, deviations for foams with differently ordered initial structures cannot be concluded, as no clear distinction becomes apparent within the investigated set.

Measuring and relating the bubble area to its number of edges has previously been proposed by Roth et al. [8]. Here, we adapt the concept and use the number of edges based parameter $\langle D_N \rangle$, which represents the mean distance between the barycentres of a bubble with N edges and its neighbours. We anticipate the mean distance $\langle D_N \rangle$ to vary with N.

Fig. 30 shows the dependency for three differently ordered structures at an equal point in their evolution. The presented data is normalized by the average distance of a six-sided bubble. As expected, the mean distance depends on the number of edges of the bubbles, and is observed to increase with N_E.

In the most homogeneous foam structure σ_0, the mean distance to bubbles' neighbours is relatively large compared to the more inhomogeneous structures. In case of the most disordered structure σ_4, the dependency of mean distance on N_E is more pronounced, and the mean distance is lower.

Throughout the foam evolution, the initial dispersity has a visible effect within the considered set of structures. Our study demonstrates that over time, the influence of structural changes on homogeneity becomes apparent through the proposed metric. To make full use of the potential of this metric, further exploration relating to different geometries and boundary conditions (such as foams in confined spaces) would be needed to observe significant divergences.

5. Conclusions

In this work, a novel numerical method based on a phase-field model for simulating liquid foam decay has been presented. This method considers gas pressure inside the bubbles, while treating it as an ideal gas. It facilitates comprehensive mapping, analysis and control of the temporal development of the decay process of foams. To represent the dynamic evolution of foam microstructure, it employs an algorithm accounting for the spontaneous rupture of foam separating films and coalescence of bubbles. The study presented herein introduces and validates the microstructure evolution model using numerical simulations. To highlight the primary capabilities of the approach, the model was applied to the systematic exploration of diverse dry foam geometries, with quasi-mono- and poly-disperse structures. By subjecting these foam structures to decay simulations driven by spontaneously rupturing films, we gain insights into how initial foam geometry and bursting probability influence the overall foam structure. Hereby, different bursting probabilities model varying rates of decay. Investigation of the foam evolution and dynamical characteristics via comprehensive parameter studies explores microstructure evolution through statistical analysis.

The numerical results indicate that the microstructure evolution in liquid foam in the dry foam limit is predicted, mapping foam decay dynamics related to successive coalescence events. Our approach adeptly accesses the intricate morphological and topological characteristics inherent in foam structures. Moreover, our framework offers insight into the complex behaviour of decaying foam through its adaptability to large-scale microstructure simulations. This allows for exploration of statistical properties, based on bubble-scale characteristics of the ensemble. With the model it is possible to specify different preconditions (such as differently dispersed initial microstructures and film bursting probabilities) precisely and individually, and to analyse their influence not only in interaction but also separately from each other. We presented comprehensible investigations of various resulting microstructure parameters, including volume, gas pressure, bubbles' shape, and connectivity, serving the purpose of outlining the model's predictive capability and describing its applicability to the investigation and in-depth analysis of foam evolution. Highlighting the critical role of each parameter for structure formation underlines the central importance of the analysis as key to the interplay of the set of parameters. In summary, the method effectively provides insight into the impact of fundamental factors governing the evolution and dynamics of decaying liquid foam. Furthermore, it successfully connects stochastic film rupture occurrences with empirical observations of the overall bubble ensemble, as demonstrated in simulated decay experiments across diverse foam morphological parameters. The presented approach consequently facilitates the implementation of predictable and tailor-made microstructures, enabling improved process control through the derivation of refined material design parameters from simulation results. Establishing links to physical units would enhance the direct applicability of this approach, potentially facilitating comparisons with experimental data. The potential of the approach unfolds in targeted materials design, as the structural parameters determine

the resulting physical properties. With the addition of physical units, this method could become a powerful tool for predicting and optimizing foam behaviour in practical applications. However, in some of the trends derived from the numerical experiments, we recognize the model's limitations, to derive potential improvements for future development. A proposed feature of a future model formulation is to include inter-bubble gas diffusion (Ostwald ripening). This process leads to gradual shrinkage and enlargement of bubbles, and influences the structural development. While the current model is based on the stochastic occurrence of film rupture, it features the flexibility to incorporate alternative probability functions as well. Future extensions could utilize this flexibility to include pressure-dependent rupture criteria, allowing for the investigation of bubble over-pressure effects on film stability and rupture dynamics in simulations.

Future work aims towards an even more integrated and realistic foam representation. These required model extensions and adaptations include incorporating coarsening and gravity in a model formulation, and coupling it with the existing framework, to further enhance its applicability. With the model constraint regarding bubbles' volume and pressures, inter bubble gas transfer (Ostwald ripening) could be facilitated by modifying this product $P \cdot V$ according to differences in pressure. The versatility of the framework provides a well-suited basis for a seamless transition to three-dimensional geometries. Future simulation studies of these 3D geometries will enable to capture the dynamics of foam decay in a new set of realizations. Also, numerical experiments could focus on investigating the influence of a wider ranging parameter set, focusing e.g. on variations in surface tension or more sophisticated initial foam geometries. Aligning the setups and results with physical units presents an opportunity for future research. Such an alignment would enhance the connection between our numerical results and experimental findings, potentially facilitating comparisons with experimental studies and enabling validation against established

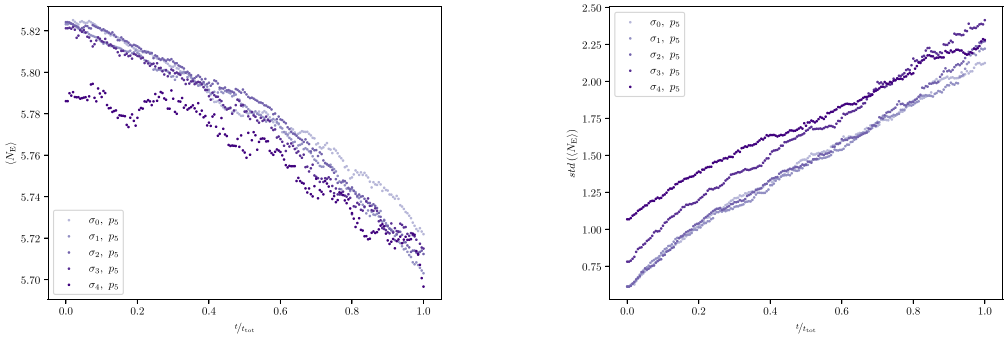

(a) Mean of bubbles' edges.

(b) Standard deviation of a).

Fig. 25. Temporal evolution of bubble edges, for different starting dispersities.

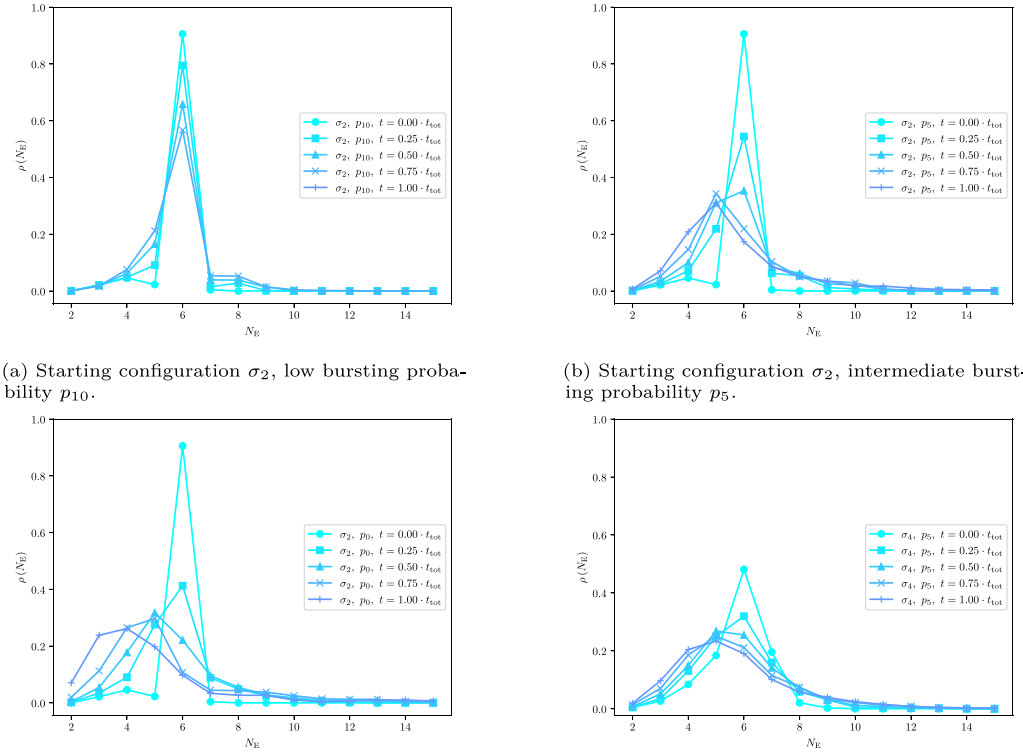

(a) Starting configuration σ_2, low bursting probability p_{10}.

(b) Starting configuration σ_2, intermediate bursting probability p_5.

(c) Starting configuration σ_2, high bursting probability p_0.

(d) Starting configuration σ_4, intermediate bursting probability p_5.

Fig. 26. Distributions of bubbles' edges. Illustration of the temporal course for different initial starting configurations and film bursting probabilities.

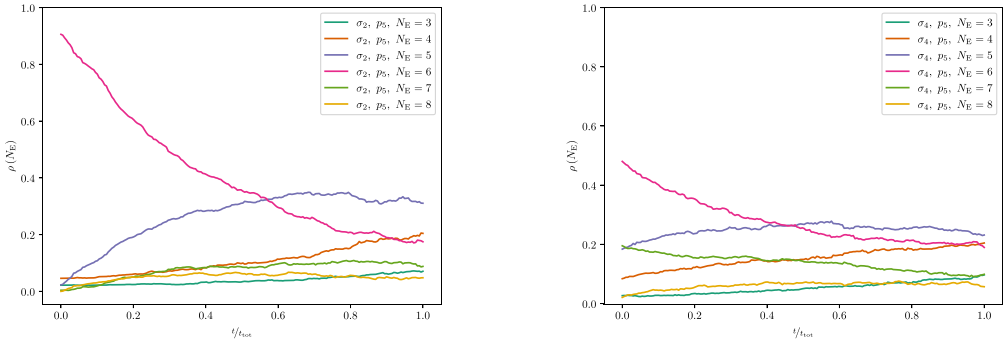

(a) Structure σ_2. (b) Structure σ_4.

Fig. 27. Details on temporal evolution of bubble edges, dissected by proportion of bubbles by edge count. Two different starting dispersities of structure.

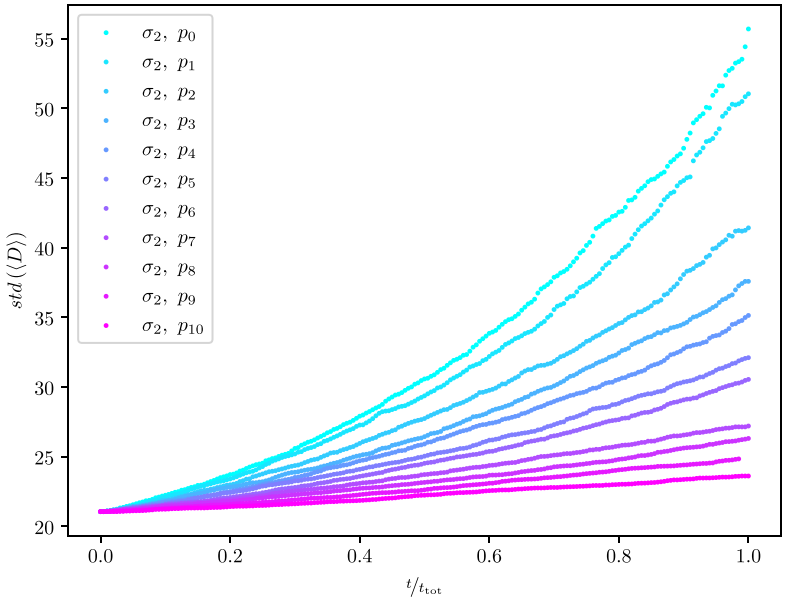

Fig. 28. Evolution of mean distance of bubble neighbours for one foam dispersity, with variable film bursting probability.

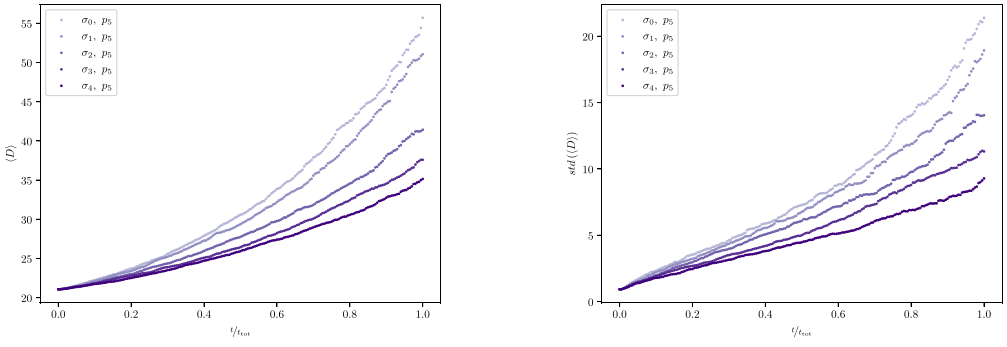

(a) Mean distance evolution. (b) Standard deviation of a).

Fig. 29. Evolution of distance of bubble neighbours for different structural dispersities, equal film bursting probability.

laws. This step could further increase the reproducibility and practical applicability of our findings within a broader context. While beyond the scope of the current study, this alignment represents a promising direction. Expanding the wetting conditions through surface tension as proposed in [32] will open up new possibilities in accessing foam with variable liquid content. We also see the opportunity to explore the evolution of foam with our framework in various specific application scenarios. Studies regarding foam geometries in confined spaces, such as porous structures, could be approached.

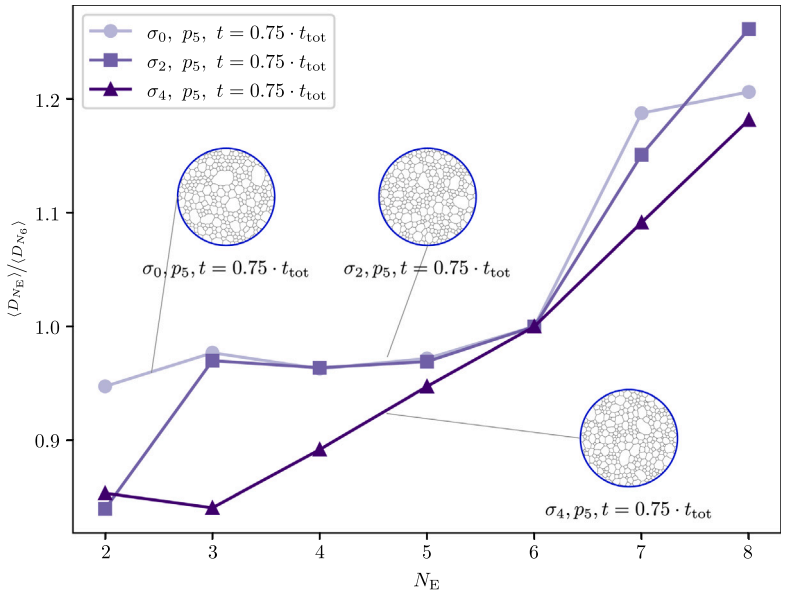

Fig. 30. Mean distance of bubble neighbours for bubbles with N_E edges, variable initial structure. Data is normalized by the average distance of a six-sided bubble.

CRediT authorship contribution statement

Jana Holland-Cunz: Writing – review & editing, Writing – original draft, Visualization, Validation, Software, Methodology, Investigation, Formal analysis, Data curation, Conceptualization. **Andreas Reiter:** Writing – review & editing, Software, Methodology, Investigation, Formal analysis, Data curation, Conceptualization. **Johannes Hötzer:** Writing – review & editing, Software, Data curation. **Anastasia August:** Writing – review & editing, Supervision, Project administration, Methodology, Funding acquisition, Conceptualization. **Michael Selzer:** Writing – review & editing, Software. **Britta Nestler:** Writing – review & editing, Supervision, Resources, Project administration, Funding acquisition, Conceptualization.

Declaration of competing interest

The authors declare that they have no known competing financial interests or personal relationships that could have appeared to influence the work reported in this paper.

Acknowledgements

The main research was funded by the Deutsche Forschungsgemeinschaft (DFG, German Research Foundation), under the grant number NE822/31-1. Contributions were supported by the Helmholtz association, Germany through the programme MSE, no. 43.31.01. This work was performed on the computational resource bwUniCluster funded by the Ministry of Science, Research and the Arts Baden-Württemberg, Germany and the Universities of the State of Baden-Württemberg, Germany, within the framework program bwHPC. The authors acknowledge support by the state of Baden-Württemberg through bwHPC. The authors thank Dr. Aron Kneer for fruitful discussion.

Data availability

Data will be made available on request.

References

[1] P. Stevenson, Foam Engineering: Fundamentals and Applications, first ed., John Wiley & Sons, Chichester, 2012.

[2] M. Reder, J. Holland-Cunz, P. Lorson, A. August, B. Nestler, Simulative determination of effective mechanical properties for digitally generated foam geometries, Adv. Eng. Mater. 25 (19) (2023) http://dx.doi.org/10.1002/adem.202300340, URL https://onlinelibrary.wiley.com/doi/10.1002/adem.202300340.

[3] C. Stubenrauch, A. Menner, A. Bismarck, W. Drenckhan, Emulsion and foam templating-promising routes to tailor-made porous polymers, Angew. Chem. Int. Ed. 57 (32) (2018) 10024–10032, http://dx.doi.org/10.1002/anie.201801466, URL https://onlinelibrary.wiley.com/doi/10.1002/anie.201801466.

[4] D.L. Weaire, S. Hutzler, The Physics of Foams, 1 publ. as, Clarendon Press, Oxford, 1999.

[5] E. Rio, A.-L. Biance, Thermodynamic and mechanical timescales involved in foam film rupture and liquid foam coalescence, ChemPhysChem 15 (17) (2014) 3692–3707, http://dx.doi.org/10.1002/cphc.201402195, URL https://onlinelibrary.wiley.com/doi/10.1002/cphc.201402195.

[6] K.J. Stine, S.A. Rauseo, B.G. Moore, J.A. Wise, C.M. Knobler, Evolution of foam structures in langmuir monolayers of pentadecanoic acid, Phys. Rev. A 41 (12) (1990) 6884–6892, http://dx.doi.org/10.1103/PhysRevA.41.6884, URL https://link.aps.org/doi/10.1103/PhysRevA.41.6884.

[7] J. Duplat, B. Bossa, E. Villermaux, On two-dimensional foam ageing, J. Fluid Mech. 673 (2011) 147–179, http://dx.doi.org/10.1017/S0022112010006257.

[8] A.E. Roth, C.D. Jones, D.J. Durian, Bubble statistics and coarsening dynamics for quasi-two-dimensional foams with increasing liquid content, Phys. Rev. E 87 (4) (2013) 042304, http://dx.doi.org/10.1103/PhysRevE.87.042304, http://arxiv.org/abs/1207.0146, https://link.aps.org/doi/10.1103/PhysRevE.87.042304.

[9] I. Cantat, S. Cohen-Addad, F. Elias, F. Graner, R. Höhler, O. Pitois, F. Rouyer, A. Saint-Jalmes, Foams, Oxford University Press, Oxford, 2013, http://dx.doi.org/10.1093/acprof:oso/9780199662890.001.0001, URL https://academic.oup.com/book/9438.

[10] B. Deminiere, A. Colin, F. Leal-Calderon, J.F. Muzy, J. Bibette, Cell growth in a 3D cellular system undergoing coalescence, Phys. Rev. Lett. 82 (1) (1999) 229–232, http://dx.doi.org/10.1103/PhysRevLett.82.229, URL https://link.aps.org/doi/10.1103/PhysRevLett.82.229.

[11] V. Carrier, A. Colin, Coalescence in draining foams, Langmuir 19 (11) (2003) 4535–4538, http://dx.doi.org/10.1021/la026995b, URL https://pubs.acs.org/doi/10.1021/la026995b.

[12] E. Forel, B. Dollet, D. Langevin, E. Rio, Coalescence in two-dimensional foams: A purely statistical process dependent on film area, Phys. Rev. Lett. 122 (8) (2019) 088002, http://dx.doi.org/10.1103/PhysRevLett.122.088002, URL https://link.aps.org/doi/10.1103/PhysRevLett.122.088002.

[13] Z. Briceño-Ahumada, W. Drenckhan, D. Langevin, Coalescence in draining foams made of very small bubbles, Phys. Rev. Lett. 116 (12) (2016) 128302, http://dx.doi.org/10.1103/PhysRevLett.116.128302.

[14] H. Ritacco, F. Kiefer, D. Langevin, Lifetime of bubble rafts: Cooperativity and avalanches, Phys. Rev. Lett. 98 (24) (2007) http://dx.doi.org/10.1103/PhysRevLett.98.244501.

[15] K. Khristov, D. Exerowa, G. Minkov, Critical capillary pressure for destruction of single foam films and foam: effect of foam film size, Colloids Surf. A 210 (2–3) (2002) 159–166, http://dx.doi.org/10.1016/S0927-7757(02)00377-1, www.elsevier.com/locate/colsurfa, https://linkinghub.elsevier.com/retrieve/pii/S0927775702003771.

[16] A.L. Biance, A. Delbos, O. Pitois, How topological rearrangements and liquid fraction control liquid foam stability, Phys. Rev. Lett. 106 (6) (2011) 068301, http://dx.doi.org/10.1103/PhysRevLett.106.068301.

[17] J.J. Chae, M. Tabor, Dynamics of foams with and without wall rupture, Phys. Rev. E 55 (1) (1997) 598–610, http://dx.doi.org/10.1103/PhysRevE.55.598, URL https://link.aps.org/doi/10.1103/PhysRevE.55.598.

[18] M. Kelager, K. Erleben, A nonlinear vertex-based model for animation of two-dimensional dry foam, in: P.R. Hilton, J. Braz, Adrian (Eds.), GRAPP 2010 - Proceedings of the International Conference on Computer Graphics Theory and Applications, Angers, France, May 17-21, 2010, INSTICC Press, 2010, pp. 296–303, doi:cbe060204df02f310b45b14a2167b5588e1ef517.

[19] K.A. Brakke, The surface evolver, Exp. Math. 1 (2) (1992) 141–165, http://dx.doi.org/10.1080/10586458.1992.10504253, URL http://www.tandfonline.com/doi/abs/10.1080/10586458.1992.10504253.

[20] N. Kern, D. Weaire, A. Martin, S. Hutzler, S.J. Cox, Two-dimensional viscous froth model for foam dynamics, Phys. Rev. E 70 (4) (2004) 041411, http://dx.doi.org/10.1103/PhysRevE.70.041411, URL https://link.aps.org/doi/10.1103/PhysRevE.70.041411.

[21] Y. Seol, Y. Kim, Numerical study on statistical behaviors of two-dimensional dry foam, Commun. Comput. Phys. 25 (1) (2019) 289–310, http://dx.doi.org/10.4208/cicp.OA-2017-0242, URL http://www.global-sci.com/intro/article_detail/cicp/12672.html.

[22] R. Saye, J. Sethian, Multiscale modelling of evolving foams, J. Comput. Phys. 315 (2016) 273–301, http://dx.doi.org/10.1016/j.jcp.2016.02.077, URL https://linkinghub.elsevier.com/retrieve/pii/S0021999116300158.

[23] T. Uehara, Numerical simulation of foam structure formation and destruction process using phase-field model, Adv. Mater. Res. 1042 (2014) 65–69, http://dx.doi.org/10.4028/www.scientific.net/AMR.1042.65, URL https://www.scientific.net/AMR.1042.65.

[24] S. Vakili, I. Steinbach, F. Varnik, Multi-phase-field simulation of microstructure evolution in metallic foams, Sci. Rep. 10 (1) (2020) 19987, http://dx.doi.org/10.1038/s41598-020-76766-z, URL https://www.nature.com/articles/s41598-020-76766-z.

[25] T.C. Lavoratti, S. Heitkam, U. Hampel, G. Lecrivain, A computational method to simulate mono- and poly-disperse two-dimensional foams flowing in obstructed channel, Rheol. Acta 60 (10) (2021) 587–601, http://dx.doi.org/10.1007/s00397-021-01288-y, URL https://link.springer.com/10.1007/s00397-021-01288-y.

[26] J. Hötzer, A. Reiter, H. Hierl, P. Steinmetz, M. Selzer, B. Nestler, The parallel multi-physics phase-field framework PACE3D, J. Comput. Sci. 26 (2018) http://dx.doi.org/10.1016/j.jocs.2018.02.011.

[27] J. Hötzer, Massiv-parallele und großskalige Phasenfeldsimulationen zur Untersuchung der Mikrostrukturentwicklungnull, KIT Scientific Publishing, Karlsruhe, 2017, URL https://www.ksp.kit.edu/9783731506935.

[28] B. Nestler, H. Garcke, B. Stinner, Multicomponent alloy solidification: Phase-field modeling and simulations, Phys. Rev. E 71 (4) (2005) 041609, http://dx.doi.org/10.1103/PhysRevE.71.041609.

[29] L.C. Evans, Entropy and partial differential equations, in: Lecture Notes at UC Berkeley, 2004, http://www.voteearlyvoteoften.us/data/books/pdf/BooksinScience/Mathematics/MathematicalPhysics/EntropyandpartialdifferentialequationsEvansL.C..pdf.

[30] S.G. Kim, D.I. Kim, W.T. Kim, Y.B. Park, Computer simulations of two-dimensional and three-dimensional ideal grain growth, Phys. Rev. E 74 (6) (2006) 061605, http://dx.doi.org/10.1103/PhysRevE.74.061605.

[31] M. Selzer, Mechanische und strömungsmechanische Topologieoptimierung mit der Phasenfeldmethode, KIT Scientific Publishing, Karlsruhe, 2014.

[32] F. Wang, H. Zhang, Y. Wu, B. Nestler, A thermodynamically consistent diffuse interface model for the wetting phenomenon of miscible and immiscible ternary fluids, J. Fluid Mech. 970 (2023) A17, http://dx.doi.org/10.1017/jfm.2023.561, URL https://www.cambridge.org/core/product/identifier/S002211202300561X/type/journal_article.